Politecnico di Torino

Université Paris Cité

INTERNATIONAL DOUBLE DEGREE PROGRAM IN:

Nanotechnologies for ICTs and Quantum Devices

Academic year 2021/2022

MASTER THESIS

Towards ultrafast and broadband integrated mid-infrared amplitude modulator

---

Author:
Lucia LUCA

Academic Supervisors:
Prof. Ricciardi CARLO
Prof. Della Rocca MARIA LUISA

Internship Supervisors:
Dr. Bousseksou ADEL
Dr. Colombelli RAFFAELE

In collaboration with:

université PARIS-SACLAY

Acknowledgements

I want to sincerely thank the Mid-IR team from the photonic departement of the Centre de Nanoscience and Nanotechnologies for the suggestions and information they gave me, for the notions they taught me and for making me feel an integral part of the group since the day one. In particular, I would like to thank Adel and Raffaele for the discussions we had, from which I had the opportunity to really learn a lot. Thanks also to all my colleagues of the C2N, with whom I had the opportunity to share so many "good" coffees.

I also want to thank and congratulate all my friends from the Nano(S)quad group with whom I had the opportunity to share so many good moments and experiences in Paris that I will always remember. Without you this experience would not have been so special.

I want to thank my family for always supporting me, for you sacrifices and for always being with me even if I was (and I still am) so far from you, especially during the university period. Thanks to all my friends, especially those from childhood, with whom I have shared and continue to share a consistent part of my life and my experiences. Thank you for always being on my side, for your advice and the long calls we have made to keep us constantly updated on what is happening to us. Finally, I want to thank all the people I have met and known over the last few years who, in one way or another, have contributed to help me on my path.

Contents

List of Figures

Chapter 1

Introduction

1.1 General context

The term *optoelectronics* refers to a branch of photonics aimed at the study, design and development of electronic devices for the generation, manipulation and detection of electromagnetic radiation. Normally, optoelectronics is closely related to the field of *integrated photonics*: it is the technology of integrating various optical devices and components for the generation, focusing, splitting, combining, isolation, polarization, coupling, switching, modulation and detection of light all on a single chip. These chips, which are generally referred to as PICs, are the optical versions of electronic integrated circuits [2], [3]. Their development was born thanks to the science and technology of semiconductors which led to the creation of the first integrated semiconductor laser diode [4]. The chip elements can be both passive (e.g. couplers, switches, modulators, multiplexers) and active (e.g. amplifiers, detectors, and lasers) and can be connected to each other monolithically using optical waveguides. They can achieve high compactness and robustness, potentially improving the operational reliability and obtaining a reduced size, weight and power consumption allowing to avoid bulky, complex, and expensive optical systems. PICs find applications in a wide variety of fields like telecommunications, biosensors for speeding up medical diagnosis, sensing and spectroscopy. In recent years, much attention has been pushed toward the optimization and improvement of the PICs components, trying also to couple them with the usual integrated electronic components, a step that would enable an important technological evolution. Although these devices are well developed for applications in specific regions of the electromagnetic spectrum, such as the visible and near infrared, in others like the mid infrared (MIR, $\lambda \sim 3 - 12\mu m$) the ability to integrate certain kind of devices is still lacking (or their performances are not satisfying), hampering the progress of Mid-IR integrated photonics. As a result, the field of applications evolves more slowly and is more limited than what it could actually offer. As a consequence much effort has been put nowadays, either in terms of material science, semiconductor device design, processing and fabrication, into filling this technological gap.

1.2 Presentation of the Laboratory

The internship takes place at the Centre de Nanoscience et de Nanotechnologies (C2N), a joint research centre between CNRS and Université Paris-Saclay, located in Palaiseau. The laboratory has expertise in both fundamental and applied research, dealing with large variety of topics such as material science, nanophotonics, nanoelectronics, nanobiotechnologies and microsystems, as well as nanotechnologies. The research activity is organised into four different departments: *Photonics*, *Materials*, *Nanoelectronis* and *Microsystems and Nanobiofluidics* departments. The work developed in the internship is carried out in the *MIR-THZ Quantum Devices* team, contained in the *ODIN* group of the photonics department. The activity of the group focuses on the development of novel optoelectronic devices in an under-developed region of the electromagnetic spectrum, i.e. from the mid to far infrared region ($\lambda \approx 3\mu m$ to $\lambda \approx 300\mu m$). The developed devices are based on intersubband transitions (ISB), the key building block behind the design and implementation of quantum cascade lasers (QCL) and Quantum Well Infrared Photodetectors (QWIP).

1.3 Internship subject: State of the art, issues and scientific objectives

1.3.1 The MIR spectral range and its applications

The mid-infrared (MIR) wavelength range represents a portion of the electromagnetic (EM) spectrum with wavelength between 3 and 12 μm (although the length of the region can depend on the considered reference). Scientific and technological breakthroughs in the MIR photonics have caused a major development of mid-infrared PICs. The invention of the Quantum Cascade Laser (QCL, [5]) has been a crucial event for MIR sources enabling a vast range of applications in the field of spectroscopy and communication. The interest in spectroscopy is ascribed to the fact that a large number of molecules undergo strong characteristic vibrational transitions in this domain thus making mid-infrared spectroscopy useful to identify and quantify molecular species in a given environment. Besides, MIR spectroscopy permits also to perform diagnostics of composite systems of physical, chemical or biological interest, in the gas, liquid or solid phase [6]. Moreover, the mid-infrared region also contains two important windows (3–5 µm and 8–13 µm) in which the Earth's atmosphere is relatively transparent. These regions can be exploited for telecommunication purposes.
In addition to QCLs, the invention of MIR cameras gave birth to thermal imaging [7]: any object behaves as a black body and emits a certain amount of radiation depending on its temperature. The spectrum of emission is peaked in the MIR region at 300K and the higher the temperature of the object, the more infrared radiation is emitted. Likewise ordinary cameras, which are capable of capturing visible light, the infrared cameras can capture photons emitted in the infrared and create an image from which the temperature of an object can be inferred. These cameras also work in the dark and for these reasons are extremely useful in medical thermography, defense, astronomy, pollutants detection, chemical imaging and many others.
Contrary to what is developed in the short wavelengths, where the components are integrated in the same chip, the Mid-IR systems are still mainly based on different devices aligned in free space. An increasing effort in the research and development community is spent to develop a new Mid-IR integrated devices. One of those integrated devices is the amplitude modulator.

1.3.2 Amplitude modulators for the MIR

All the recent advances stemmed from the development of transformative optical components. In fact, besides the detection and generation of light, another paramount functionality for any PICs is the possibility to electrically control the amplitude, phase and polarization state of an optical beam up to ultra-short time scales. This task is performed by the modulators.
Among all the modulators, those on which this project wants to focus are the amplitude modulators. The concept of amplitude modulation is rather old and is broadly used in the field of electronics: it consists in impressing the information of the signal to be transmitted in a carrier signal by modifying its amplitude. A well known application, commonly used in everyday life, is the broadcast of radio programs.
In the field of MIR photonics, fast amplitude and phase modulations are useful for a large variety of applications like laser amplitude/frequency stabilization, coherent detection, spectroscopy and sensing, modelocking, optical communications, military countermeasures and many others [8]. To date, the fastest modulation speed (20-30 GHz) has been obtained by direct modulation of MIR QCLs: direct modulation means that the signal is modulated before being emitted by the laser, i.e. the current, before reaching the laser, is modified with the desired signal for the application of interest. However, a solution of this kind requires complex design and elevated injected power [8],[9] and it can also cause a degradation of the laser stability.
To avoid direct modulation, in the visible and near-infrared, the solution has been found in modulators that are physically separated from the laser source. An external modulation can bring several advantages like a better flexibility to photonic design, preventing the degradation of the laser stability and linewidth and at same time minimizing the simultaneous occurrence of amplitude and frequency modulation, as well as ameliorated and flatter modulation bandwidth. Although these results are already well established for the visible and near infrared, this technological solution does not exist in the MIR, hampering the progress of the MIR PICs both in terms of integration and systems deployment.
My internship is taking part of a starting research funded project *"Bird"* that gathers three french research labs C2N, IEMN (Lille) and LPL (Villetaneuse). The main goals of this project are to build ultrafast, broadband ($1 \sim 40$ GHz) and integrated amplitude and phase modulators for the MIR spectral range, that will be capable of addressing the needs of emerging MIR photonics applications and platforms. The devices will be optimized to operate for wavelengths around 8.5 µm, in the center of the second infrared atmospheric transparency window and thus ideal for spectroscopy purposes and free-space optical communication. The

amplitude modulator (AMD) will be useful in applications like AM spectroscopy, gas sensing, amplitude modulated energy efficient communication systems and many others, therefore capable of filling the technological gap in the context examined above.

1.3.3 Device concept

An amplitude modulator has two important figure of merits: bandwidth and modulation depth. The bandwidth is defined as the range of modulation frequencies over which the device can be operated. By convention, the bandwidth of a modulator is usually taken as the difference between the upper and lower frequencies at which the modulation depth falls to 50% of its maximum value. Instead, the modulation depth is defined as the ratio between the transmitted intensity of the signal with and without the applied bias [3]. Nowadays there are few commercially available MIR MDs but they are either bulky and narrowband: a bulky Ge acousto-optic MDs operating up to $\lambda \sim 10$ µm with narrow bandwidth (1 MHz∼100 MHz)[10] and narrowband (∼100kHz) electro-optic modulators based on GaAs or CdTe [11]. The direct modulation of QCLs (up to 20GHz, [12]), cited in 1.3.1, is thus justified by the fact that these MDs cannot reach GHz of modulation bandwidths. Hence, there is the need to design and realize a device that allows to obtain these desired performances.
The physical concepts on which the idea of the device is based are those of the intersubband transitions and dielectric waveguide (labeled ISB and WG respectively. Physical discussion can be found in Appendix A). A MIR dielectric WG, whose task is to guide and confine the electromagnetic radiation to be modulated, is placed on top of a metallic plate which serves as ground electrode. A second electrode is placed on top of the waveguide that behaves as a gate and will define the length of the MD. The two metallic plates are the electrodes at which the modulating signal will be injected. A sketch of the device is shown in Fig.1.1. The active region is based on a system of repeated coupled quantum wells (repetition of AlGaAs/GaAs QWs) and it will be inserted in low refractive index vertical cladding layers to provide the vertical confinement while the lateral confinement is achieved using air.

ISB transitions are at the heart of the operating principle of QCLs and QWIPs (see subsection 1.3.1) and they occur in multiple quantum well structures, where, thanks to band gap engineering, it is possible to confine the electrons in proper ways. Semiconductor technologies allow for superior control over the construction of multiple quantum wells (MQWs). In particular, the ability to modify the thickness of the QWs allows to change the absorption wavelength at will, whereas the ability to choose the type and concentration of doping allows to modify the strength of the absorption. These two phenomena permit to have a high level of control in the design of the device. The basic idea is to work with two coupled QWs, one doped and the other undoped. The whole structure will be designed in such a way that, when the modulating signal is not applied, the device does not absorb photons.

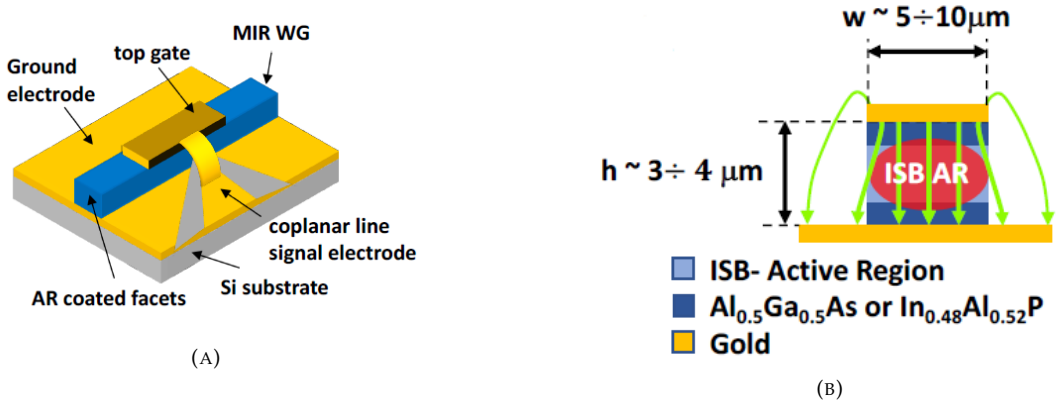

FIGURE 1.1: Sketch of the integrated amplitude modulator based on ISB active region in an integrated MIR dielectric waveguide. (A) General vision of the device; (B) Device input/output facet.

This can be obtained by doping only one of the two coupled QWs (which will act as a carrier injector, a reservoir. The doped QW is the wider one) while the undoped one (the thinner one) is constructed to absorb the radiation at the desired frequency. At zero bias, there are no carriers in the undoped QW so the

structure is transparent. However, when the applied voltage is not zero, there will be an injection of carriers from the doped QW to the undoped one thanks to the quantum tunneling effect. This process allows to populate the fundamental level of the undoped QW which will begin to absorb the radiation impinging on the device. A sketch of the band diagram of the coupled QWs that describes the absorption process is shown in Fig.1.2. The speed of the modulation will depend mainly on two factors: the tunneling time

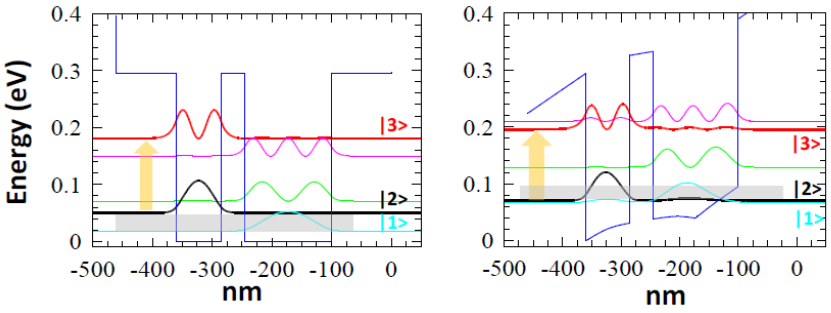

FIGURE 1.2: Sketch of the band diagram of a coupled QWs system to show the basic working principle of the AMD. In both figures are depicted the square modulus of the wavefunctions to visualize the allowed states in the two quantum wells. On the left: unbiased system. The QWs are designed so that the transition (yellow arrow) occurs between the black and red levels. The grey line is the Fermi level of the structure. With no bias, only the cyan level is populated hence no absorption can occur. On the right: biased structure. Black and cyan level anticross hence electrons can tunnel on the black level and they can absorb the photons jumping on the red level.

and the RC constant of the device. Since the tunneling time is very fast, of the order of picoseconds, the final speed is limited by the RC constant and the capacitance must be minimized as much as possible. The final device will contain a periodic repetition ($\sim$20/30 periods) of the two coupled QWs. The insertion of the active region inside of a dielectric waveguide allows to have, in the limit of reasonable doping level, a greater overlap between the MIR field and the MQWs, hence increasing the absorption in the "on" state. Since in the "off" state the device does not absorb light, even complex passive circuits can be integrated on a chip together with the AMD. Key points of the design will consist in trying to decrease as much as possible the losses of the WG and to avoid a possible overlap between the field in the WG and the metallic electrodes that will cause consistent dissipation. The modulation depth can in fact be measured just by characterizing the WG losses at the output facet with and without the applied bias on the MD. To ensure the correct operation of the device, low-loss WGs are necessary, with maximum transmission when the MD is in the off-state. The analysis of this last point will be central in the work developed in the internship, since it is the first requirement for the success of the project.

1.3.4 State of the art

The physical concepts on which the device is based are well developed and have solid foundations. For what concerns the amplitude modulator, although the topic was initially addressed in the 90s [13], [14], [15], [16], it was subsequently abandoned and there have been no further developments since then. These first works have been done mostly in transmission geometry, i.e. without inserting the active region in a waveguide but using the so called Brewster angle (i.e. the angle that matches the TM polarization). This choice is driven by the selection rules imposed by the ISB in a MQWs structure (i.e. only TM polarized light can trigger the ISB transitions, see A.1.2) but a transmission geometry produces a dramatic consequence on the performance of the device: the modulation depth is rather small ($\approx$ 0.13%, [13]) because of the very reduced overlap between the field and the active region, regardless of the doping. The only work that has been done in a waveguide geometry is reported in [13]. In any case, only the DC analysis has been performed, without taking into account the speed of the device and, moreover, the voltage to be applied to obtain a satisfactory modulation is extremely high ($\sim$ 40V). The voltage must be much smaller for operational purposes. The maximum working voltage will depend on the geometry of the waveguide, on the amount and kind of doping, on the geometry of the active region and on the choice of the materials. In principle it is also possible to work with a maximum of 8V. An additional drawback is that the device, even

in off-state, absorbs the EM radiation thus making it not very useful for applications. Different approaches have been recently investigated: modulation based on transition between strong/weak coupling regimes [8] and Stark effect modulators [17] have been latterly published but both devices rely on free space application and they do not investigate the integrated waveguide geometry.
The challenges to be faced do not only concern the modulator: the waveguides must exhibit remarkably low losses in the MIR and this is difficult to achieve. Being able to build low-loss MIR integrated waveguides will not only be one of the most important points for the success of the project but will be useful for all the III-V MIR PICs field. To best of our knowledge, the best results in this field have been obtained in [18] and [19]. The considered structures in these works are dielectric waveguides in InGaAs/InP or fully suspended AlGaAs with losses lower than 2 dB/cm ($0.46 cm^{-1}$), but in both works the study has been limited up to 5µm, well below the frequency range of interest proposed in the project. Furthermore, at 8.5µm, the problem of waveguide losses will be more consistent because of the residual doping that triggers the free carriers absorption (appendix A.2).
Ultimately, being able to achieve the objectives of the project, succeeding in overcoming the above-mentioned limits, is an exceptional scientific challenge with potential results and benefits that can go far beyond building the device alone, but also help the entire MIR scientific community.

1.4 Organization of the work

During the internship the work has been organized in such a way to guarantee a deep understanding of all the key points involved in the design of the modulator. It is worth to notice that the project has been launched just this year therefore fundamental aspects, such as the components for the optical set-up and the alignment of the components themselves have been developed from scratch. Furthermore, it is important also to underline that this activity is part of a much wider project (*BIRD project*) for which a doctoral study is envisioned. The work is divided in two main sections: a theoretical section and an experimental section.

Theoretical part

The problem has been divided in its building blocks, each of which has been analyzed separately. The study was carried out focusing on three different aspects: the *dielectric waveguide*, the *band structure of the modulator* and the *optical properties of the modulator*. Because of organization reasons, the team went ahead with the work starting to manufacture waveguides in InGaAs/InP on which the optoelectronic characterization will be carried out to determine the waveguide losses. These samples were used as a starting point to study the losses and the confinement of the electromagnetic field as a function of the geometry, doping and the coupling losses with an external laser source (a QCL emitting at 8.5µm, the same source that will be used for experimental measurements). The simulation work was carried out using Lumerical's MODE and FDTD solvers, a commercial software developed specifically for design and investigation of photonic components for PICs. To validate them, the results of the simulations will then have to be compared with the experimental outcomes and will also serve to understand how to design and optimize the MIR waveguides to ensure low losses and maximum input coupling, a paramount aspect for the success of the project. At the same time, through the use of a home-developed code, the band diagram of the active region was simulated to understand its physics and the key points of the design. In addition, using a theoretical approach that allows to describe the coupling between the ISB and the electromagnetic radiation, a model describing the dielectric function of the device has been developed to be included in Lumerical for the electromagnetic simulation of the amplitude modulator inserted inside the waveguide. Since the optical properties of the modulator are not independent on the band diagram but are completely determined by it, the two simulations will be interconnected. In the end, a complete model to fully simulate and design the amplitude modulator should be available to the group and, with these first results, the first decisions in terms of design and optimization will be undertaken by the group.

Experimental part

Two main experimental activities that have been carried out during my internship were the fabrication of the InGaAs on InP substrate passive device, the characterization of the building blocks elements of the injection/collection setup and first alignment steps. These activities will be detailed on chapter4 and chapter 2. The injection experiments should take place at the very end of the internship. It is important to notice that this experimental setup will be used as a part of long term PhD project.

Chapter 2

Fabricated samples

As first internship activity, passive optical waveguides have been fabricated. The core waveguide is made of 3µm thick $In_{0.53}Ga_{0.47}As$ layer lattice matched with an unintentionally InP doped substrate. The WGs are divided into 4 groups, each of which contains 4 waveguides with different geometry. The groups differ according to the length of the waveguides: the main idea is in fact to measure the losses as a function of length and geometry. The height of all the guides is 3 µm, while there are four different widths: 3,5,10 and 15 µm. The values chosen for the overall lengths of the guides are: 0.247, 0.303, 0.383 and 0.503cm. As visible in Fig.2.1b, the length is varied by changing the straight section between the two bent parts. The input and output facets of the WGs are linked to 100µm long linear tapers with a rectangular input section of (100x3x100)µm as dimension. Linear tapers are necessary to increase the input coupling when the laser source is focused on the input facet of the device.

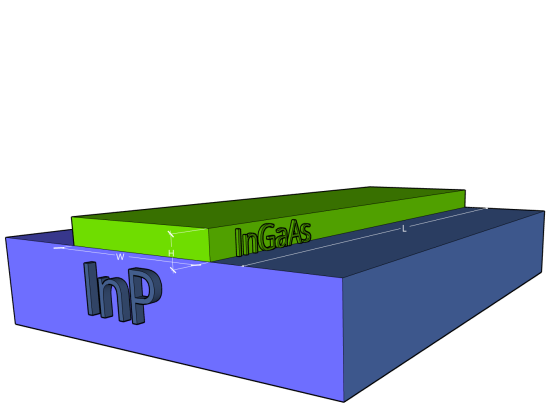

(A)

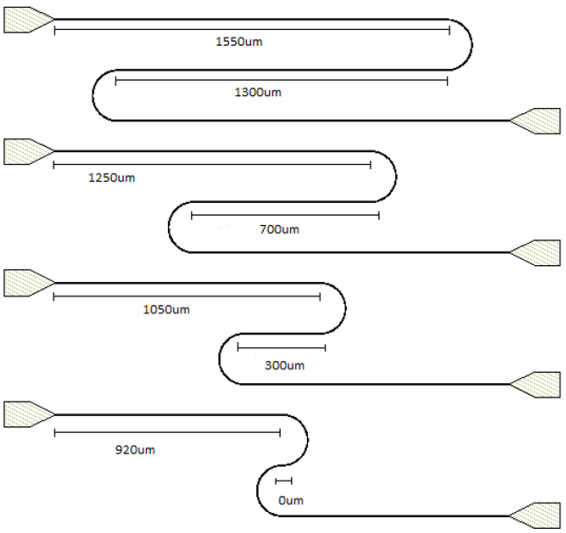

(B)

FIGURE 2.1: Schematics of the dielectric waveguides. (A) A strip waveguide geometry; (B) Mask used for the e-beam litography.

Experimentally speaking, to avoid that the laser source focused at the input is on the same trajectory as the objectives used for measuring the transmission of the waveguide, the waveguides are not straight but curved, so as to avoid the alignment between the input and output objectives which can cause artifacts in the measurement results. As mentioned in appendix A, the presence of curves induces losses that will be investigated in detail with the simulations to understand how to design them adequately. The substrate is thick enough to be considered infinite and thus avoid the effects of losses and imperfect confinement.

Fabrication. The substrate is InP on which was epitaxially grown $In_{0.53}Ga_{0.47}As$ (MBE deposition). On top of the InGaAs, 500nm of Si_3N_4 was deposited with PECVD. This layer serves as hard mask during the etching process required to obtain the final devices. The patter of the mask, attached in Fig.2.1b, was realized using electron beam litography. To perform the litographic step, it was necessary to deposit PMMA

A6, a positive resist, on top of Si_3N_4. Then, the e-beam litography was performed. After the resist development, 40nm of Cr have been deposited by means of e-beam evaporation, followed by lift-off. The pattern was transferred to the Si_3N_4 with RIE (SF_6:CHF_3), where the Cr served as mask. To obtain the WG structure, the etching of the $In_{0.53}Ga_{0.47}As$ was performed with ICP-RIE (Inductively Coupled Plasma Reactive Ion Etching, HBr:O_2), during which the residual Cr has been removed and Si_3N_4 served as hard mask. Afterwards, the Si_3N_4 was removed with Fluoride based chemistry, in particular using the BOE, a buffered HF solution. A further cleaning of the sample has been done using plasma O_2 to remove dust and contaminants. In the end, by following the right crystallographic orientation, cleaving has been perform to isolate each group of WGs as function of their width. Because of the shortness internship period and the safety training needed for cleanroom facilities at C2N, the fabrication steps were handled by hosting group members where I attended to the different fabrication steps.

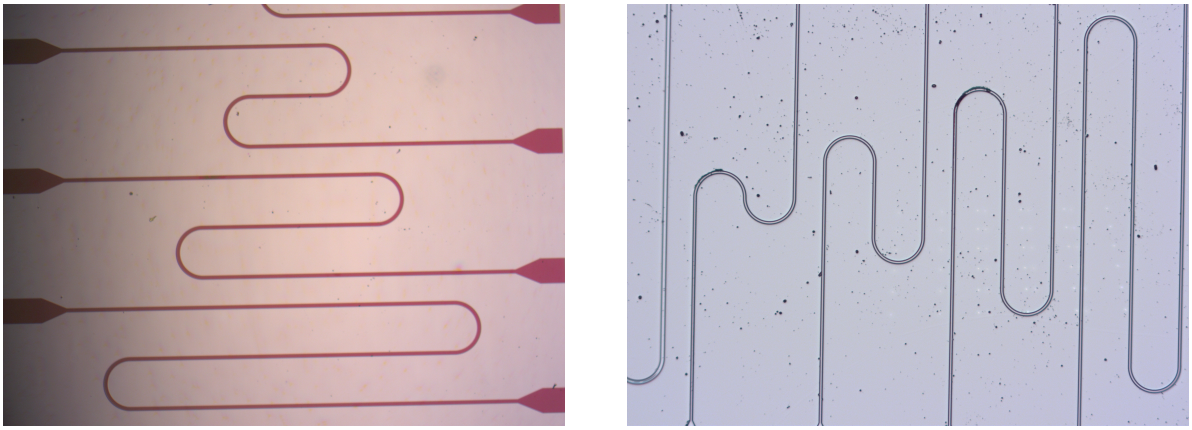

FIGURE 2.2: Optical microscope images before (left) and after (right) the ICP etching of the WGs.

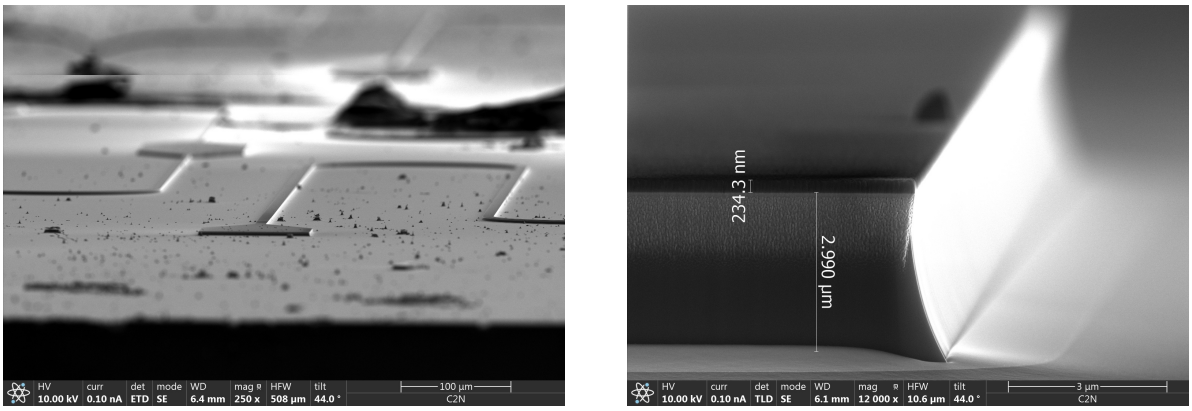

FIGURE 2.3: SEM images of the WGs after the ICP etching.

Chapter 3

Electromagnetic simulations of the waveguides

In this chapter the simulations carried out to evaluate the overall losses of the samples described in chapter 2 will be examined: it will be necessary to evaluate the losses of the straight sections, described by the absorption coefficient per unit of length α; the losses due to the curved sections and the coupling losses due to the coupling with the external laser source which occurs through the linear tapers and the evaluation of the input/output coupling losses.

3.1 Modal analysis: determination of the input mode

First of all, it is necessary to know what are the modes that can be propagated inside each waveguide. The questions to be answered are basically three: how many modes can the WGs support? How is the confinement of each mode? In the case of monomodal WG, is the fundamental mode TE or TM? The parameters on which attention must be focused are essentially two: the TE polarization fracion and the effective refractive index. The first one is a measure of how close the considered mode is to an ideal TE mode. It is useful because normally in real WGs the modes cannot be strictly classified as TM or TE but they can be also a mixture of the two, hence they will be TE-like and TM-like modes. In the following, with *TE modes* we mean all modes with a TE polarization fraction close to 1 while with *TM modes* all modes with TE polarization fraction close to 0. The second one, labeled n_{eff}, is a measure of what the phase delay of light propagating in a specific WG mode would be compared to that of light in the vacuum. n_{eff} can give hints on the confinement of the mode: a mode will be guided if its effective refractive index is higher than the refractive index of the surrounding materials, otherwise it will escape down into the substrate or in the top cladding material.
To obtain these information, 2D simulations on a cross section of the waveguides have been performed by means of the MODE Solver software from Lumerical and its FDE – finite difference eigensolver [20]. It solves the Maxwell's equations by formulating them into a matrix eigenvalue problem and uses sparse matrix techniques to calculate the spatial profiles of the possible propagating modes. In order to run the simulation it is necessary to define a simulation region, also labeled as *mesh*, namely a discretization of the spatial domain in a grid in whose nodes the Maxwell's equations are solved. The choice of the boundary conditions (BCs) becomes important at this point: usually, to compute the eigenmodes of the structure, metallic BCs are enough to obtain reliable results. However, the definition of the simulation region must be done carefully to avoid numerical artifacts in the final outcomes.

3.1.1 Simulation settings

The first step to do is to define the materials of which the structure is made. Since the working wavelength of the modulator is 8.5µm, these first simulations were carried out at 8.5µm, hence no dispersive analysis has been performed with the refractive indexes considered as values and not functions of the frequency. The core material is $In_{0.53}Ga_{0.47}As$, with refractive index n=3.4 while the substrate material is InP with refractive index n=3. The surrounding material is air with n=1. The working area is defined on the xz plane (y direction is the propagation direction). The studied WGs have a structure of 3x3, 5x3, 10x3 and 15x3 μm^2 (note: $w \times h$ notation is $width \times height$ of the WGs) according to the samples shown in chapter 2. The simulation region is attached in Fig.3.1. In order to increase the accuracy of the final result, it is possible also to put a finer mesh override on the region of major interest (in this case the core of the WG), as visible in the reported figure.

FIGURE 3.1: FDE simulation region. On the right, the mesh is made visible.

3.1.2 Convergences of the results and numerical stability

When doing numerical simulations, it is critical to do convergences tests. This ensures that the simulation is free from numerical artifacts. If the EM field is non zero at the border of the simulation region (more precisely if it is not smaller than at least 10^{-6}V/m), because of the metallic BCs, it can be reflected back by the metal and it can interfere with the simulated field in the core. This can cause artifacts that must be avoided to have reliable analyses. To get rid of them, it is necessary to perform convergences studies. These studies were made verifying that the field was actually negligible on the edge of the simulation region. In order not to unnecessarily burden the calculation, the smallest region that satisfies this requirement was chosen. In fact, the best trade-off between accuracy and computation time must always be sought. The dimension has been chosen as (40x20)µm which is sufficiently large to guarantee reliable results. Another convergence test should be performed on the dimension of the mesh cells: a certain degree of stability is necessary to trust the results of the simulation. Hence, the decision on the mesh cells size, that is the fineness of the mesh, for the override region was based on a convergence test. The effective indices n_{eff} for the fundamental TE and TM modes were used as the figures of merit, that is, the parameters that ought to converge. To determine the cells dimension, sweeps on mesh override refinements were performed with 0.05µm$\leq$ dr $\leq$1µm (where dr=dx=dz is the mesh cell size). In the end, with a uniform mesh override of dr=0.08µm around the core, n_{eff} has a variability of $10^{-3}$with further mesh refinements.

3.1.3 Results

3x3 µm^2 waveguides

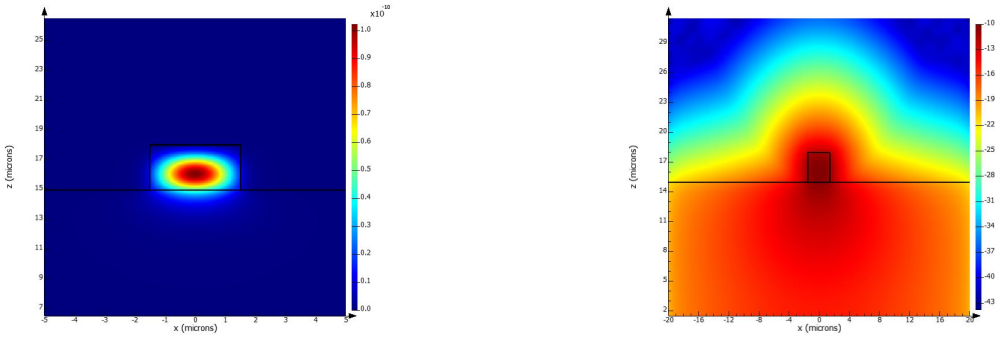

(A) (B)

FIGURE 3.2: Poynting vector as a function of position in W/m^2 of the TM fundamental mode in the 3x3µm WG. (A) Plot in linear scale; (B) Plot in logarithmic scale to better see the penetration (the window is wider than the one in picture (A) to better visualize the field distribution).

The simulation results show that the 3x3 guide is single-mode TM. However, the confinement is rather poor: this can be seen by looking at the n_{eff}=3.029 that, compared to the substrate n=3, means a large

penetration of the field in the substrate of the WG. This penetration is clearly visible by looking at the power distribution in logarithmic scale as shown in Fig.3.2. By integrating the power contained in the core and dividing it by the power contained in the entire simulation region, just the 77% is contained in the core. Moreover, due to the fact that the mode in the guide occupies all the entire core area and therefore it has a strong overlap with the surfaces of the core, it is likely that the scattering losses in this guide are greater than in the others due to the huge interaction between the mode and the surface of the core. As it will be clear later, the features of this mode will induce enormous losses in the bent sections.

5x3 µm^2 waveguides

The situation is much better in the 5x3 WG, where the confinement of the field is much more improved because of the increased dimension of the core. About 85% of the power is contained in the core. Besides, the guide has two allowed modes, one TE and one TM. Since for the modulator and the ISB physics it is necessary to fulfill the ISB selection rules, it is necessary to work with TM modes, hence only the properties of these modes will be considered in the following. The TM mode has n_{eff}=3.132 and can be seen in Fig.3.3.

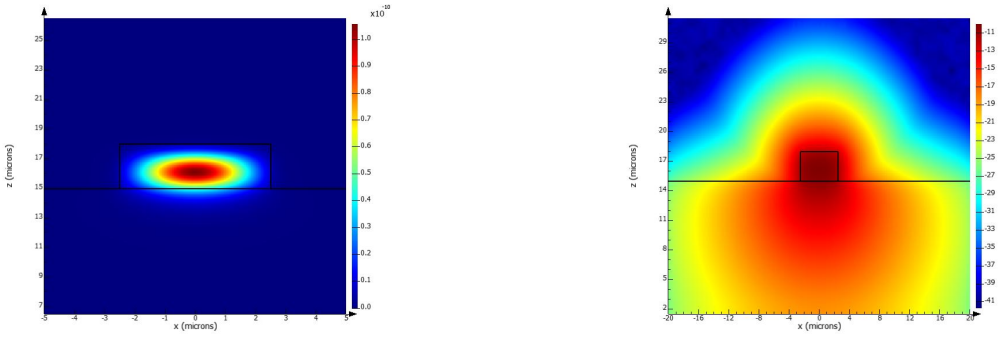

(A) (B)

FIGURE 3.3: Poynting vector as a function of position in W/m^2 of the TM fundamental mode in the 5x3 µm WG. (A) Plot in linear scale; (B) Plot in logarithmic scale to better see the penetration (the window is wider than the one in picture (A) to better visualize the field distribution).

10x3µm^2 and 15x3µm^2 waveguides

Considering just the fundamental TM mode, the 10x3 structure has 86% of the power contained in the core while the 15x3 has a confinement of 87%. Moreover, the larger becomes the width, the higher will be the number of the modes allowed in the structures. 10x3 and 15x3 structures are in fact multimode WGs, with the first one allowing for 2 TM modes and 3 TE modes and the second one allowing for 4 TM modes and 4 TE modes. The 10x3 fundamental TM mode has $n_{eff} = 3.189$ while the one of the 15x3 is $n_{eff} = 3.202$, both higher than the ones of the 3x3 and 5x3 structures. The higher the core area, the better the confinement. However, the fact that they are not monomodal WGs will cause dramatic problems in the design of the bends.

3.1.4 Modal analysis and doped WGs

To obtain preliminary information on the possible losses of the WGs, the FDE solver was used to calculate the imaginary part of n_{eff} of the modes, from which it is possible to trace the absorption coefficient per unit length α, which describes the exponential attenuation of the optical power of the guided mode. It will depend both on the mode and on the doping of the materials. As already described in section A.3, free carriers absorptions scale as λ^2 so at 8.5 µm even a small percentage of doping can drastically interfere with propagation and WG performances. For preliminary analysis, a doping of $5{\cdot}10^{16}$cm^{-3} has been considered in either the core and the cladding (that should be an upper bound to the background doping coming from the fabrication processes). The imaginary parts of the materials refractive indeces have been computed using a Drude model and the values are $\mathcal{N}$= 3.388+i0.000525 for InGaAs and $\mathcal{N}$=2.993+i0.000305 for InP.

Once the imaginary part of n_{eff} has been determined, α can be evaluated as:

$$\alpha = \kappa \frac{4\pi}{\lambda} \tag{3.1}$$

where κ=Im{n_{eff}}. It can also be expressed as dB/cm just by multiplying α by 4.34. The obtained values are:

- 3x3 WG: $\alpha = 7.414 cm^{-1}$
- 5x3 WG: $\alpha = 7.638 cm^{-1}$
- 10x3 WG: $\alpha = 7.606 cm^{-1}$
- 15x3 WG: $\alpha = 7.589 cm^{-1}$

These results are very high and far from the desired values of $\approx 1 cm^{-1}$. This is the reason why it is necessary to decrease as much as possible the background doping coming from the fabrication processes and it is a clear example of how important free carriers absorptions are at such large wavelengths.

3.2 Time domain analysis

To make in-depth analyses on the different waveguides, 3D FDTD simulations were carried out using Lumerical [20]. The objective is to compute again the absorption losses of all the 4 types of WG but exploiting the time evolution of the fields which in general gives much more reliable results than the MODE solver. The results are then compared with the ones presented in 3.1.4.
Finite Differences Time Domain (FDTD) is a method to solve the electromagnetic wave equation in the time domain based on the finite-differences approximation. Unlike other methods working in the frequency domain, FDTD allows to study the field evolution in time, thus including transients. It solves the Maxwell's curl equations in non-magnetic materials:

$$\frac{\partial \vec{D}}{\partial t} = \nabla \times \vec{H} \tag{3.2}$$

$$\vec{D}(\omega) = \varepsilon_0 \varepsilon_r(\omega) \vec{E}(\omega) \tag{3.3}$$

$$\frac{\partial \vec{H}}{\partial t} = -\frac{1}{\mu_0} \nabla \times \vec{E} \tag{3.4}$$

where H, E, and D are the magnetic, electric, and displacement fields, respectively, and $\varepsilon_r(\omega)$ is the complex relative dielectric function of the medium. In three dimensions, the electric and magnetic fields have 3 components each. However, by assuming an infinite dimension along the direction of propagation and that the components do not have a z-dependence (where z is the propagation direction), the Maxwell's equations split into two independent sets of equations composed of three vector quantities each of which can be solved in the x-y plane only. These are termed the TE (transverse electric), and TM (transverse magnetic) equations. These sets of equations are discretized using central-difference approximations to the space and time partial derivatives. Afterwards, the electric field vector components in a volume of space (i.e. in the so called Yee cell) are solved at a given instant in time; then the magnetic field vector components in the same spatial volume are solved at the next instant in time; and the process is repeated until the simulation time is fully evolved. In addition, in each step, there are updates at the boundaries and from the source. This is essential to extract and inject energy from/in the simulation region.

3.2.1 Meshing

The domain is meshed with a rectangular cartesian mesh. The fundamental simulation quantities (material properties and geometrical information, electric and magnetic fields) are calculated at each mesh point. As for the MODE solver, a finer mesh allows to increase the accuracy but with a substantial cost in terms of simulation time and memory requirements. In the following simulations, a conformal mesh, that allows to have still reliable results but even with relatively coarse mesh, has been used. The mesh can be made non uniform, in particular it can be done finer in proximity of the regions where the fields have strong gradients.

3.2.2 Simulation settings

First of all it is necessary to define the length of the WGs. In order to compute the losses due to free carrier absorption and to compute α, a sweep on the length as been performed. The main reason is that, since α is independent on the length, the calculation of the coefficient for different lengths allows to see if the simulation is reliable and if the result can therefore be trusted.

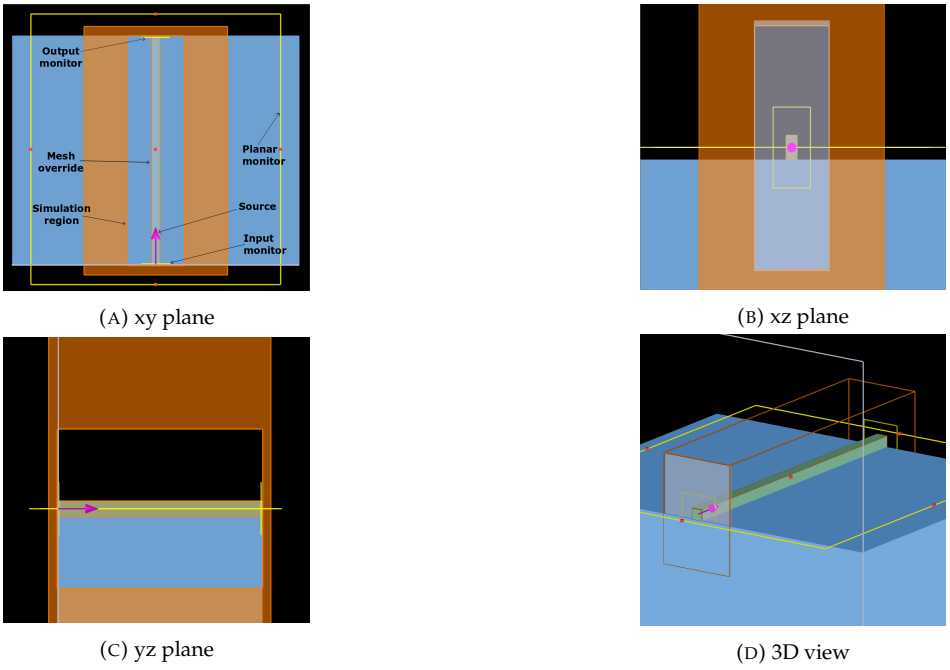

(A) xy plane

(B) xz plane

(C) yz plane

(D) 3D view

FIGURE 3.4: FDTD simulation region.

The WGs length was swept between 50,60,70,80,90,100,150 and 200µm. The simulation dimension is 30µmx20µm, decided after convergences analyses (see 3.2.3). In Fig.3.4 it is shown the simulation domain and the mesh of the structure. When running FDTD simulations, it is necessary to define the following parameters:

- **Mesh accuracy**: defines the fineness of the mesh. It is an integer number from 1 to 8, where 1 is low accuracy, and 8 is high accuracy (smaller mesh);
- **Mesh override**: inserted around the core as already done and discussed for the MODE solver;
- **Simulation time (fs):** defines the length in fs of the simulation. It should be defined according to the length of the structure, namely the radiation must be able to travel from one extremity of the structure to the other one;
- **Boundary conditions:** there are different kind of BCs that can be chosen. The one that are useful for the analysis of the losses are the PML (perfectly mathced layers), namely the boundaries absorb electromagnetic waves incident upon them. They essentially model open (or reflectionless) boundaries. PML boundaries are basically implemented as an absorbing material that is also impedance matched to the surrounding materials, to minimize reflections. An ideal PML boundary produces zero reflections, however, in practice, there will always be small reflections due to the discretization of the underlying PML equations, leading to instabilities. There are several kinds of PML boundaries essentially differing in numbers of layers. The number of PML layers should be fixed with convergences studies: an increased number decreases the reflections but increases the computation time;
- **Source:** defines the way in which the power must be injected in the simulations. In all the analyses, two kind of sources have been used: *mode source* and *gaussian source*. The *mode source* can excite a specific eigenmode of the structure. Even if it is not realistic, it is useful to understand how a mode

can be propagated and how it changes according, for example, to the geometry. A *gaussian source* defines a beam of electromagnetic radiation propagating in a specific direction, with the amplitude defined by a Gaussian cross-section of a given width. The waist radius has been taken equal to 15µm and the injection axis as the y axis. The center frequency of the two sources is 8.5µm with 0.1µm of span. It is also possible to define the polarization of the injected wave. In the following analyzes, a TM polarized wave has always been injected, both with *mode source* and *gaussian source*.

- **Frequency-domain field and power monitors:** are simulation objects that, placed in specific points of the simulation (see Fig.3.4a), save the data of the fields and power across the section covered by the monitor. They are used in the post-processing and data analysis.

The α coefficient has been computed by performing the ratio between the power detected by the monitor at the output facet divided by the one detected at the input facet. In order for the data to be comparable, the two monitors must have exactly the same size, namely 3µm wider than the WG height and WG width. Hence:

$$\alpha = -\frac{1}{L} \ln\left(\frac{P_{out}}{P_{in}}\right) \tag{3.5}$$

where L is the length of the WG in cm.

3.2.3 Convergences

To ensure results free from numerical artifacts, several convergences studies have been carried out. A test structure was used to do these studies, that is, the structure that in preliminary simulations has given more problems, i.e. the (3x3x50)µm WG, with $5{\cdot}10^{16} cm^{-3}$ as doping concentration. The simulation region has been defined with the PML layers coinciding with the input and output facets of the WG (hence y span equal to WG length, Fig.3.4c). It is used to absorb all the radiation that arrives at one end of the WG avoiding a Fabry-Perot cavity-like behavior. The x and z span have been decided with sweeps on the dimension: tails of EM fields should not overlap with PML boundaries to avoid reflections. The chosen dimension (on x and z plane) is (50x50)µm. The source used is the *mode source*, whose dimension is chosen equal to the simulation one to be sure that the eigenmode solver computes the working mode on the entire structure and not just on a part of it. The absorption coefficient has been computed for the fundamental TM mode of the WG, i.e. the mode that has been injected.
A sweep has also been performed on the number of PML layers to see the variability of the final result. With 30 layers or more, the order of magnitude in the change of α was 10^{-3} leading the PML layers to be set equal to 30. The results should not be dependent on the choice of mesh accuracy, as already said in section 3.1.2, hence mesh accuracy and mesh override sweeps have been performed to check the variability of the computed loss with the fineness of the mesh. The mesh override sweep in Fig.3.5b has been performed with a mesh accuracy of 2. Working with 1 as mesh accuracy and mesh override of 0.1µm is sufficient to

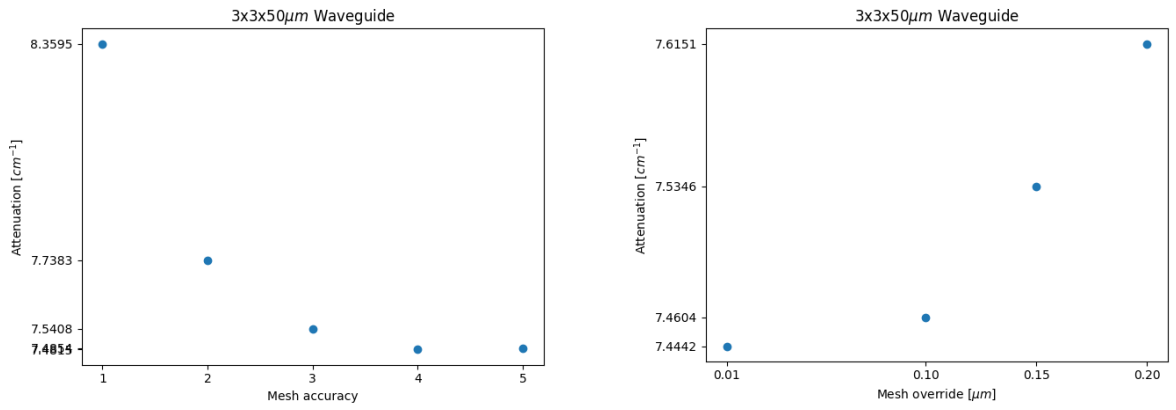

(A) (B)

FIGURE 3.5: Convergences studies. (A) Mesh accuracy sweep with no mesh override; (B) Mesh override sweep with accuracy fixed to 2.

have reliable results. This is due to the fact that, with a defined mesh override on the core area, the mesh accuracy does not change the value of α since it is completely determined only by the mesh override itself. This can be easily checked by fixing the override and doing sweeps on the mesh accuracy. The variability of α was of the order of 10^{-4}. Consequently, a mesh accuracy equal to 1 allows to lighten the computational effort, while making the mesh finer just in the core.

3.2.4 Results

With 30 PML layers, a simulation region of (50x50xL)µm, a mesh accuracy 1 and mesh override of 0.1µm, simulation time of 4000fs and mode source of dimension (50x50)µm exciting the fundamental TM mode of each WG, the results obtained are similar to the ones shown in Fig.3.6. Even if they are not exactly the same, the results obtained are in good agreement with those shown in section 3.1.4.

The fact that the calculated values are almost perfectly aligned denotes the reliability of the simulation. This flatness is common to all the investigated geometries.
The simulated values of free carriers absorption losses for the 4 types of waveguides are:

- 3x3: $7.4655 cm^{-1}$;
- 5x3: $7.6892 cm^{-1}$;
- 10x3: $7.6616 cm^{-1}$;
- 15x3: $7.6530 cm^{-1}$;

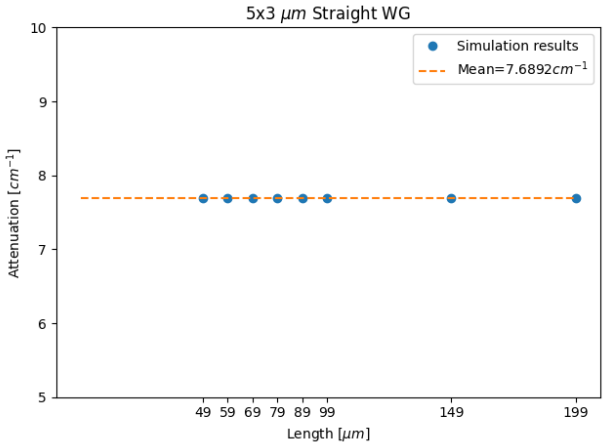

FIGURE 3.6: Example of absorption coefficient computation for the analyzed waveguides. In the picture it is attached the α of the 5x3 µm waveguide. Notice: the values of lengths are the distances between the input and output monitors, positioned 0.5µm away from the input and output facets, hence the effective length is 1µm smaller than the nominal one.

From the FDTD and MODE simulations of WG losses emerges that the doping must be very small to have reasonable values of losses. With α around $7 cm^{-1}$ the transmission is still not compromised but in order to have a good transmission and very long structures, it should be around or even smaller than $1 cm^{-1}$. Very long structures can in fact be useful to increase the coupling with the laser, a problem usually faced in the design of tapers. Long tapers imply better transmission. However, if the structure has $\alpha \approx 7 cm^{-1}$, the situation becomes dramatic because the power that actually manages to enter the WG turns out to be very very small. Consequently, optimizing the transmission of the tapers could lead to the opposite result, that is, to compromise it. The most important information that is obtained from this analyzes is that the absorption losses are not dependent on the geometry of the waveguide (unlike the confinement factors) but are almost entirely determined by the doping concentration. Different situation is obtained for the bending losses, where the geometry plays a predominant role.

3.3 Bent Waveguides

After evaluating the losses of the straight sections, it is necessary to study the physics of curved guides in detail, since all the waveguides in the real samples have bends with 100µm of radius.
The problem of the design of curved WGs has been extensively examined since 1969 ([21],[22], [23], [24] to name a few). Bent waveguides are the key building blocks of many PICs components like delay lines in Mach-Zender interferometers, WGs grating routers, Y branches, MMIs or simply another cascaded bend thus it is necessary to design them with the best possible performances. Two main factors contribute to the propagation characteristics of a bent WG: pure radiation losses and transition losses occuring between the straight and the bent sections [24]. Radiation losses are due to a distortion of the field inside of the bent section. Moreover, it is also possible that the incoming light couples with high order modes. In monomode WGs, these higher order modes are leaky modes, i.e. modes immediately below the cut-off

that have a complex propagation constant but still can propagate for long distances maintaining a profile almost fixed, hence the losses are further enhanced. In addition, because of the fact that straight and bent WGs have different eigenmodes, a non unitary overlap factor between the incoming field and the allowed modes inside of the bent WG can introduce important losses due to mode mismatch. In straight WGs, the tendency for light to diffract is compensated by the jump in the refractive index between core and cladding and the WG mode has flat phase fronts. In bent WGs, the phase fronts rotate around a rotation center. Since the group velocity of the phase fronts cannot exceed the local light velocity (c/n), there is a point where the phase front bends and the radiation of the guided mode occurs.

3.3.1 Simulation settings

Before starting with the simulations it is necessary to carry out the convergence analyses again. However, due to the fact that the simulation region and the device are much larger than the simple straight guide seen in the previous cases, these convergence studies were done within the limits of the hardware of the used PC. Convergences studies led to choose a simulation region of (120x30x120)µm, mesh accuracy 2 and mesh override of 0.2µm with 0.7µm of buffer around the core. A simulation time of 7000fs and stabilized PML BCs (namely 42 PML layers) were also chosen. The source is a *mode source* object exciting the fundamental TM mode of each WG and its dimension was chosen as (40x0x30)µm, wide enough to be sure that the field is at least 10^{-6}V/m at the borders of the source region.

Have a look at Fig.3.7 to see the structure, the positions of the source and monitors. As already done for the straight WGs, the PMLs touch the input and output facets to avoid Fabry-Perot like-behavior. Moreover, the override region cannot be done curved but it can assume just rectangular shapes, hence a finer mesh in useless parts of the simulation domain have been imposed with detrimental effects on the simulation time (that in fact is between 8 and 9 hours). It was thus necessary to find a compromise between the setting and the simulation time to allow for a mesh of the order of $\lambda/20$, roughly 0.1µm, to have reliable results. The compromise led to choose 8 layers of PML and PML just on xy plane, with metallic BCs on the z direction; 0.1µm of mesh override on the core and no buffer; simulation region of (120x30x120)µm (direction of propagation taken on xy plane); source dimension (40x0x30)µm. Likewise to section 3.2.2, the absorption coefficient has been computed by performing the ratio between the output and input power detected by using proper input and output monitors with the same dimension. In particular:

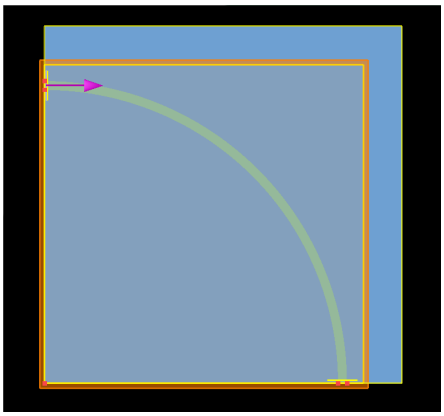

FIGURE 3.7: Simulation region for bent WGs along xy plane.

$$\alpha_{bend} = -\frac{1}{R\theta} \ln\left(\frac{P_{output}}{P_{input}}\right) \tag{3.6}$$

where R is the radius of the osculating circumference of the bend in cm and θ is the angle of the bent section in radiants. Since the coefficient does not depend on θ at fixed R, it was sufficient to simulate the 90° bend.

3.3.2 Results

The study focuses on losses due to geometry alone and not to absorption, hence no doping has been considered. The losses due to absorption can be added later by simply knowing the length of the curved section and multiplying that length by α of the relative structure calculated previously in section 3.2.4.
From a theoretical point of view [21], the losses should depend exponentially on the bending radius. The first simulations were made to check if the losses showed such a trend. In fact, using a 90 degree bend, the losses exponentially decay with an increment in the bending radius (testing the losses for R=30, 50, 70, 100 and 200 µm). This was checked on all the 4 types of WGs. It is thus necessary to design WGs with very large radii otherwise the propagation would be compromised (e.g. for the 10x3µm WG with R=50µm $\alpha_{bend} = 36.96cm^{-1}$). It is interesting to have a look at the planar distribution of the electric field throughout

the structure as resulted from the FDTD simulations for all the 4 WGs geometries and also the field distribution at the output facet. It is worth to notice that from FDTD, radiation losses and losses due to mismatch are computed simultaneously, hence the final coefficient α_{bend} includes all these factors.

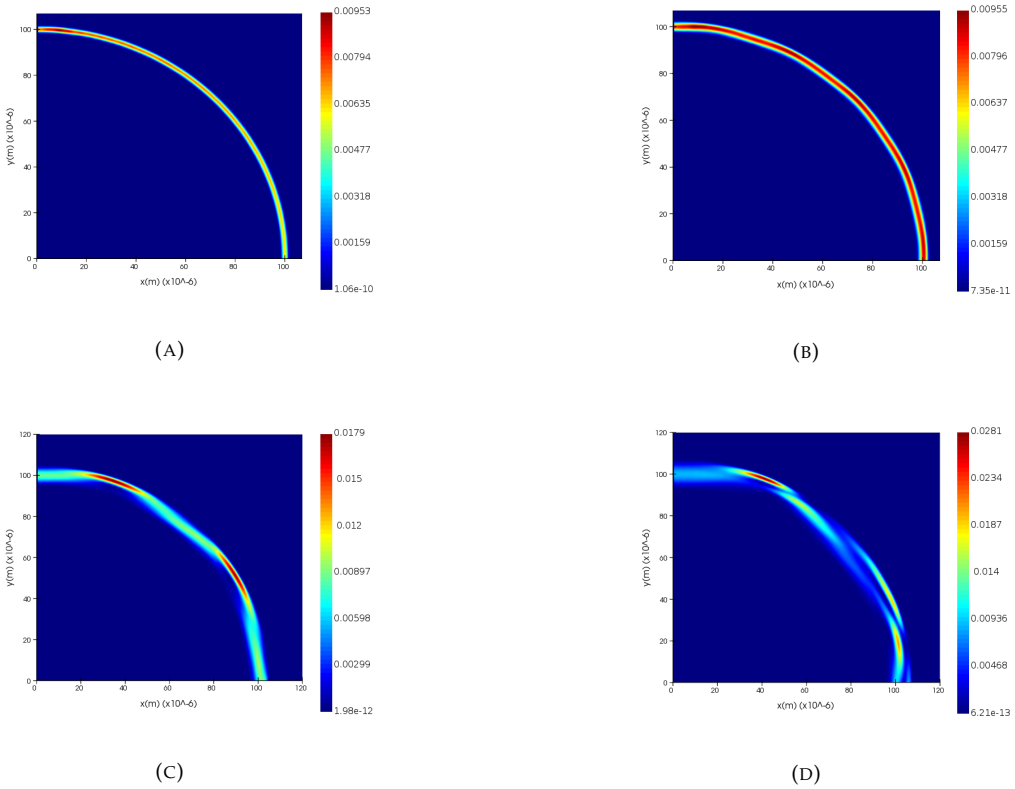

FIGURE 3.8: Poynting vector as a function of position along xy plane in W/m^2 for the four bent waveguides. (A) W=3µm; (B)W=5µm; (C) W=10µm; (D) W=15µm.

From Fig.3.8 it is clear how the field is distorted inside of the bent section. As wider is the waveguide, as stronger will be the distorsion. In particular, the distorsion is critical for the 10x3 and 15x3 structures while it is absent in the 3x3µm WG and slightly visible in the 5x3µm one. It is in fact visible that the field is displaced outwards with strong interference effects in particular in the 15x3µm structure. These interferences are ascribed to the excitation of higher order modes: light coming inside of the bent section can in fact couple to higher order modes. The 3x3 and 5x3 are monomode TM while 10x3 and 15x3 are multimode hence the excitation of higher order guided modes is possible. If this excitation occurs in the 3x3 and 5x3, leaky modes will be excited and thus the only effect would be to increase the losses. In the case of 10x3 and 15x3, with the excitation of guided higher order modes, the dynamics of the device can be completely changed, particularly if there are more cascaded bent sections, leading to undesired device behavior (besides, the losses are function of the modes and higher modes usually have smaller confinement factor, thus higher losses).

The excitation of higher order modes is more evident if the electric field profile is analyzed at the output facets. In particular, a straight section has been added at the output in order to analyze the modes excited in it, right after the bent section. The results are attached in Fig.3.9c and Fig.3.9d where it is clearly visible a second mode at the output facet. Due to the fact that the WGs are wide, they can host several guided TM modes and this feature leads to power exchange between the fundamental and higher order modes, with consequences on the device losses. An important check, useful in the context of the modulator, is to verify the polarization of the field coming out from the bent section: a flip in the polarization must be avoided in order to couple to the ISB transitions that occur in the modulator. The computation of the TE polarization fraction at the output facet of each WG was hence evaluated. The results confirm that the output fields are all TM (TE polarization fraction almost zero for all the four WGs), implying no polarization changes, i.e.

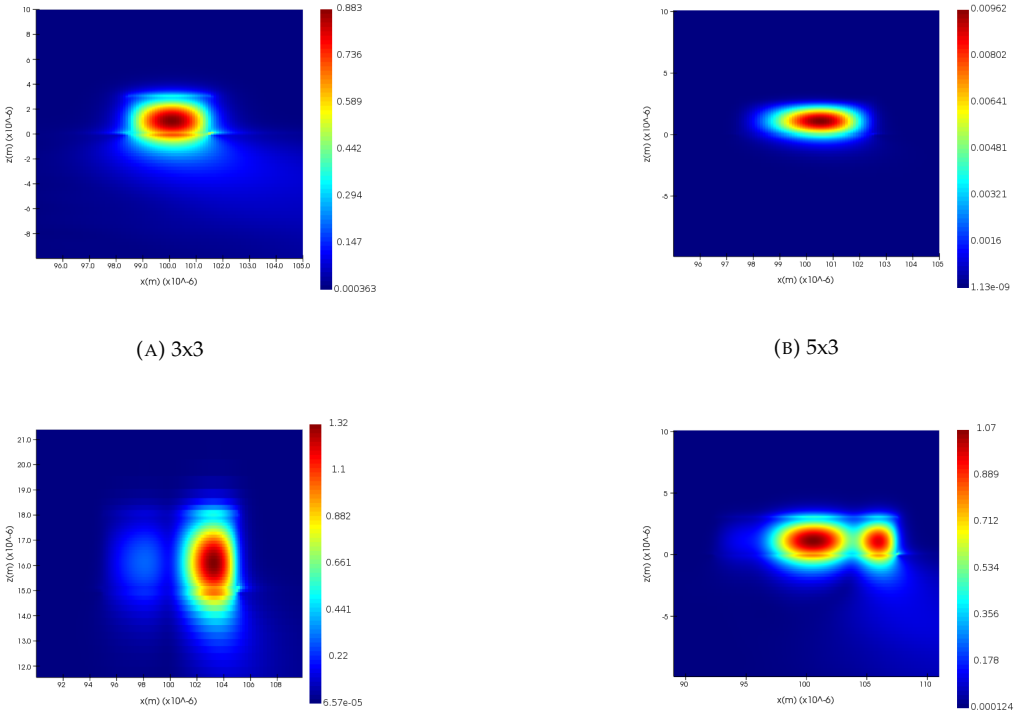

(A) 3x3

(B) 5x3

(C) 10x3

(D) 15x3

FIGURE 3.9: Electric field amplitude at the output facet of the bent waveguides measured in V/m.

power is exchanged only between modes with same polarization.
The results of the bending losses computation are attached in Table.3.1. At this point, combining the absorption losses and losses due to bends, the total losses per each WG of the samples described in chapter 2 can be estimated. The obtained values are summarized in Table3.1, where are also included the transmission coefficients of the entire WGs. The computation of the overall losses has been done using the following expression:

$$T = \frac{P_{out}}{P_{in}} = e^{-\alpha_{absorption}\cdot(L_1+L_2+L_3+2R\theta)} e^{-\alpha_{bend}\cdot 2R\theta} \tag{3.7}$$

where L1,L2 and L3 are the lengths of the three straight sections of each WG sample (see Fig.2.1 in chapter2).

TABLE 3.1: Total WGs losses

	Absorption coefficients		Transmission coefficients			
WGs[µm× µm]	$\alpha_{absorption}[cm^{-1}]$	$\alpha_{bend}[cm^{-1}]$	L=0.503cm	L=0.383cm	L=0.303cm	L=0.247cm
3×3	7.4655	14.6	0.93%	2.29%	4.16%	6.32%
5×3	7.6892	2.11	1.83%	4.61%	8.52%	13.11%
10×3	7.6616	4.13	1.64%	4.10%	7.57%	11.63%
15×3	7.6530	5.2	1.54%	3.85%	7.1%	10.9%

Data analysis. As one might expect, the shortest guides are the ones that transmit the most, i.e. the ones with L=0.247cm. The reason is ascribed to the free carrier absorptions in fact, the longer the structure, the

stronger the absorption and the smaller the transmission.

By analyzing in detail the transmission of each geometry, it is noteworthy how small is the transmission of the 3x3µm WG. This must be ascribed to the value of α_{bend} ≈14cm^{-1} rather than $\alpha_{absorption}$. As mentioned in section 3.1.3, the profile of the mode occupies the whole core area and the confining is rather poor, with a non negligible penetration in the substrate. Hence, as soon as it is displaced outwards, a large part of the power is radiated despite the large bending radius. This means that R=100µm is not sufficiently large to have low losses for the 3x3µm and it must be further increased. Among all the WGs, the best one is the 5x3µm WG with the lowest bending losses. A possible explanation can be ascribed to the increased core area and an ameliorated confinement of the mode, together with the fact that it is a monomode waveguide. A good compromise between smallness of the core area (i.e. small field distortion in the bend) and confinement factor is achieved in this sample.

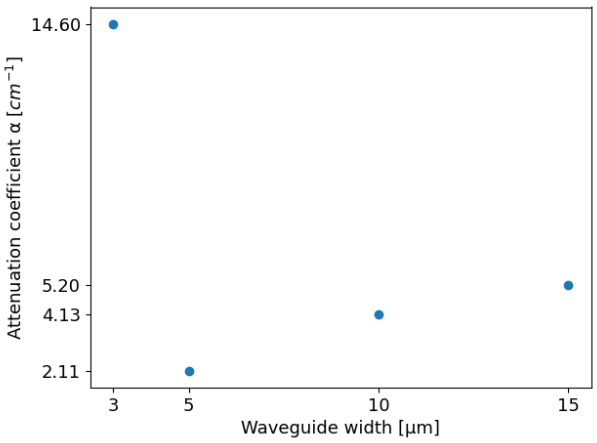

FIGURE 3.10: Summary of the attenuation coefficients for the simulated bent waveguides as function of the waveguide widths.

The 10x3µm WG shows an increased bending loss, due to the excitation of the second guided mode and to the field distortion (note: the excitation of the second order mode is less important than the 15x3µm WG). The 15x3µm structure has the highest bending loss because of the distortion and the strong excitation of the second guided mode.
Although the 5x3 µm WG seems to be a good sample (because it is monomodal TM and has a small α_{bend}), the value of bending losses are still high and far from the desired values: they should be much more negligible when compared to $\alpha_{absorption}$.

Hints from 2D MODE analysis. To better understand the results attached in the table, MODE simulations were carried out on the curved section to examine the contribution and profile of each mode in the bends. It is necessary to underline that the numerical values obtained from the MODE solver are not reliable as the ones obtained from the FDTD solver but they can give hints in understanding the physical rationale behind the trends of the data attached in the latter table.
To perform the simulation, PML BCs have been used to be able do detect the radiation losses. A simulation region of (40x30)µm with a mesh override of 0.1µm around the core with 0.7µm as buffer have been used as simulation settings. In addition, the 2D simulation allows also to compute the overlap factors between the different modes, to have an idea about how the power redistributes itself between the guided modes in the bent section.
The simulation for the 3x3µm WG shows that the losses are entirely determined by the radiation losses of the fundamental TM mode. The result (also quantitatively) is similar to the one obtained from the FDTD solver. The overlap factor between the fundamental TM mode of the straight section and the eigenmode of the bent section is almost unitary, and is an additional confirmation of the predominance of the radiation losses as main cause of the transmission worsening. For what concern the 5x3µm WG, the radiation losses are negligible for the fundamental TM mode and also the overlap factor is almost unitary. The computation of the overall losses gives a value that is close to the FDTD simulation. The small field distortion, together with an improved confinement and almost unitary overlap factor is what gives to this geometry the best value of α_{bend} among all the investigated samples. For the 10x3µm WG, the fundamental TM mode has non zero overlap with the first and second TM guided modes of the bent section. The fundamental mode has negligible radiation losses due to the good confinement, the increased core area and also to the bending radius, which makes the distorsion of the field negligible. Different is the situation for the second guided TM mode, that shows a poorer confinement and also an increased effective area if compared to the fundamental one. This implies that the field has a stronger distortion and higher radiation losses with respect to the fundamental one. The 15x3µm WG exhibits the same feature of the latter WG: the input field excites both the fundamental and second guided TM modes of the bent section. The improved radiation losses are

ascribed to the second guided mode and not to the fundamental TM one.
In conclusion, to avoid a derimental effect of the bends on the WGs transmission, it is essential to make a precise and accurate design of the curves, being careful to avoid higher order modes excitation and a strong field distorsion.

3.3.3 Design solutions

Differently from the straight WGs, where the only tricky point to take care of is the doping coming from the fabrication processes, in the bent WGs the situation is much more complicated and requires a careful and subtle design. First of all, a common issue to all bent WGs is the mode mismatch at the interface between the straight and the bent section, leading to scattering events. There are two solutions to avoid this phenomenon: the first one is to laterally offset the straight WG relative to the bent WG in order to obtain a better mode overlap; the second one is to vary continuously the curvature using for instance Euler's spirals rather than using abrupt bends [22]. While the former one can partially solve the problem concerning the overlap factors leaving unaffected the radiation issues due to the strong distortion of the field in the bend, the latter solution is preferred because it can also be useful in avoiding the field distortion and also the excitation of higher order modes since the transition is smoother and the overlap factors with other modes (including the leaky modes) are reduced. A different design solution could be the matched bend [23]. It is noteworthy that the excitation of the leaky modes can occur also at the output of the bend, namely when the field goes back into the straight section. This is completely detrimental if more bends are cascaded (like in the actual samples of chapter 2). When the field enters in the bend it preserves its shape but during the propagation, since the different excited modes have different phase velocities, it is distorted. Nonetheless, after a beat length L_b defined as $2\pi/(\beta_{b1} - \beta_{b2})$, with β_{b1} and β_{b2} the phase constants of the bent modes, the two excited modes return in phase and the shape of the injected mode is recovered. A matched bend is when the length of the bend is a multiple integer of L_b. The result is that transition losses vanishes and the output field, attenuated only by radiation (that must be small), is undistorted and can propagate unaffected in the straight section. For the next simulations, the idea would be to focus only on the 5x3 WG that is a good starting point and see how the structure can be ameliorated to decrease further the overall losses and, if needed, make changes to the geometry and move to more efficient structures. This design solutions will be implemented in the last two months of the internship and are not included in this report.

3.4 Coupling losses

Since in the experiments the coupling will be realized by focusing the laser on the input facet of the WGs, proper linear tapers have been fabricated to increase the coupling efficiency (chapter 2). A taper is a smooth transition between two waveguides of different widths or height and is used to couple two components with different waveguide geometry. Changes in the waveguide structure result in mode conversion. This means that power is exchanged between the different modes of the waveguide. Mode conversion can be suppressed when the change in waveguide structure is very gentle. In this case we call the adaptation of the mode profile *adiabatic*. An adiabatic transition between two waveguide structures is a transition where the mode of the system adapts to the changing geometry without loosing power by conversion to other modes.
The tapers in the samples are linear and they have a length of 100µm and height of 3µm, with an input waveguide of (100x3x100)µm as dimension. The first task was to evaluate the coupling losses using FDTD simulations.

Simulation settings. The FDTD region has a dimension of (250x70x300)µm; mesh accuracy of 2; stabilized (i.e. 42 layers) PML on x,y and z and simulation time of 8000fs. No mesh override was used around the structure (because of memory requirement issues). A gaussian source with $\lambda = 8.5$µm, 0.1µm of λ span, a waist radius of 15µm and with a TM polarization has been used to inject the power. To simulate the injection, it was positioned in air at 40µm from the device (to understand the choice of the source features have a look at section 4.1).

Several monitors have been used to analyze the field distribution in different points of the structure both in the transversal plane and in the longitudinal plane to the direction of propagation. In addition, to calculate the reflections due to the index jump between air and InGaAs and InP, a monitor was placed behind the source to measure the percentage of power reflected by the WG. An example of the field distrubution along the structure is shown in Fig.3.12.

(A) (B)

FIGURE 3.11: FDTD simulation region for coupling losses analyses. (A) xy plane view, where y is the direction of propagation; (B) 3D view of the simulation region.

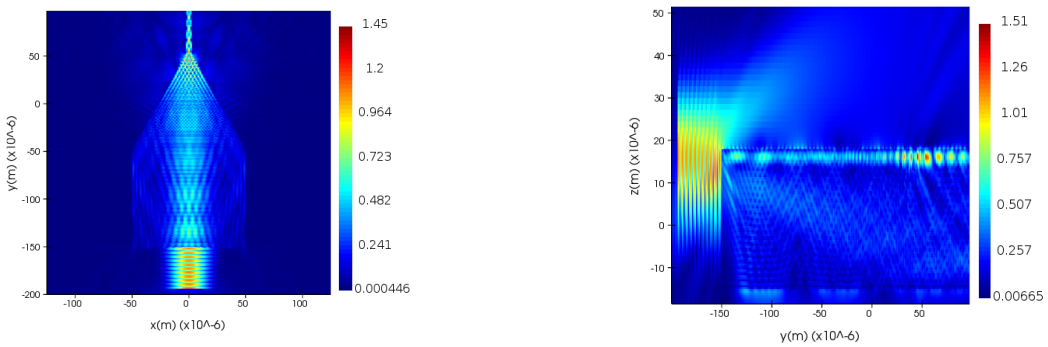

(A) (B)

FIGURE 3.12: Time averaged electric field amplitude in V/m. (A) planar view (xy plane) in the middle of the core; (B) lateral view (xz plane) in the middle of the structure. y axes is the direction of propagation.

Results. Since the laser beam waist radius is 15µm while the height of the WG is 3µm, lot of power is lost above and below the guiding structure. This is clearly seen in Fig.3.12b, where the electric field propagates both in the air and within the substrate. Of the power that enters the core, part is lost by irradiation as can be seen in Fig.3.12a. Another fraction of power is instead lost because of the reflections at the facet of the WG. The transmittance of the structure is obtained by performing the ratio between the power flowing through a monitor at the output of the WG with the same dimension of the core divided by the input power of the laser. The computed values take into account all the sources of losses listed above. The transmissions are:

- 3x3: 2.4%
- 5x3: 2.9%
- 10x3: 6.9%
- 15x3: 10%

The values increase as the width of the WG increases because of the fact that the taper angle Ω decreases (angle defined in Fig.3.13). The value of the reflected power is instead the 13% of the overall power. The transmission of the structure is very poor hence it must be optimized. The optimization process is rather complicated to be performed with FDTD simulations: the overall 300µm-long structure requires almost 12 hours to be simulated. Consequently, the optimization has been carried out using a combination of FDTD and MODE solvers. The *mode expansion* monitors of the FDTD simulations were used to understand which modes are excited within the taper input. Basically, the mode expansion monitors compute the eigenmodes

of the structure in a certain section and then, to compute the excited modes and the power percentage shared among them, they compute the overlap factors between the eigenmodes and the fields saved in a specific *frequency-domain field and power* monitor. The result is that the overall power excites the fundamental TM mode of the rectangular input. The same check has been done on the WGs in order to see which modes are excited once the field reaches the WGs core. For the 3x3 and 5x3 all the power is sent in the fundamental TM. For the 10x3 and 15x3 the power excites the fundamental TM modes, with a negligible (yet non zero) power that is sent in the second TM guided mode.
The optimization process has been done with the MODE solver just on the 5x3 structure since, from the results of sections 3.3.2, it is the best WG of the fabricated samples. By exciting the fundamental TM mode of the structure, it is possible to examine the parameter S_{21}, which describes the transmission of the fundamental TM mode of the taper input into the fundamental TM mode of the WG. The idea is to optimize the coupling process by working on this parameter. The power lost because of the bigger dimension of the gaussian beam with respect to the waveguide core is not solvable, while the reflections can be reduced by designing a proper antireflection coating to be inserted on the input facet (a task that will be performed in the second part of the internship). There are three degrees of freedom for the optimization: the length of the taper, the width of the input and the shape of the taper. For what concern the shape of the taper, the possibilities are basically three and are shown in Fig.3.13. The equation that descibes the shape is the following:

$$w(x) = \alpha(L - x)^m + w_2 \tag{3.8}$$

with $w(x)$ the profile of the taper, $\alpha = (w_1 - w_2)/L^m$, w_1 and w_2 as reported in Fig.3.13. In particular, four different cases have been examined: m=0.3, m=0.5, m=1 and m=1.5, each of which has been tested in the interval L=[50µm, 1000µm] divided in 101 points and at four different widths of the input: w1=100µm, w1=70µm, w1=50µm and w1=35µm.
The results of the optimization are attached in Fig.3.14.

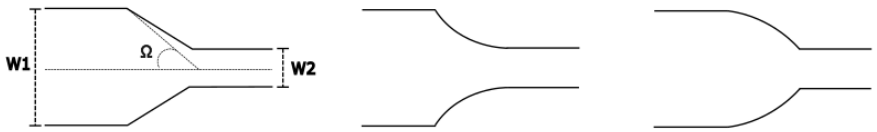

FIGURE 3.13: Profile of tapers according to equation 3.8. The parameter defining the shape is m. (Left) m=1; (Center) m<1; (Right) m>1.

It is clear how an increment in the length, regardless of the value of m, induces an increment in the transmission of the structure (because taper angle Ω decreases as the length is increased). It is worth to notice that 1mm long tapers are useless if one takes into account the free carriers absorption. Consequently, a change in the taper's shape is required as additional degree of freedom.

Transmission as a function of m does not have a well-defined behavior and in general there is no detectable pattern. The best trade-off would be to achieve the greatest possible transmission with tapers that are not too long to comply with absorption losses. However, a trend can be identified by examining the transmission as a function of the input width W1: the smaller W1, the higher the transmission, even with short tapers. In fact, what really matters, is the ratio between W1 and W2: the more the ratio tends to one, the higher is the transmission because of the decreased taper angle Ω. Then we can modify m in a proper way to find the maximum in the transmission. It makes no sense to further decrease W below 35µm otherwise the size of the taper would be laterally smaller than the laser beam size and the losses would increase not due to internal transmission but to the quantity of light that can be conveyed inside the structure.

In Fig.3.14a, the transmission exhibit strong oscillations for m=1.5 and m=1. A possible explanation is associated with a probable mode conversion: if instead of examining only the first fundamental TM mode of the taper input, the first 2 TM modes are analyzed and their transmission is studied, where there is a minimum of the transmission of the first mode there is a maximum in that of the second mode and vice versa. This does not cause any modification on the excited mode in the waveguide input but could involve a different overlap factor between the taper mode and WG mode and consequently greater losses. In fact,

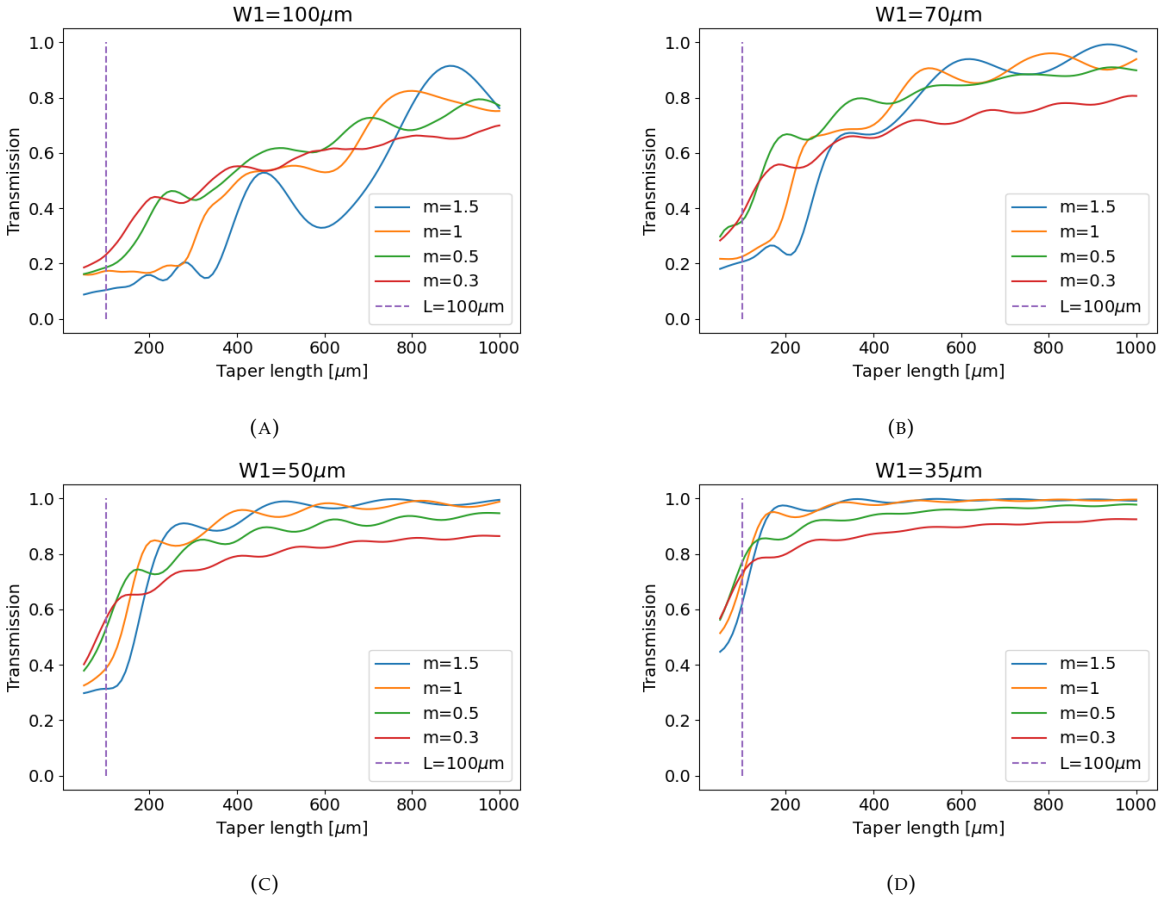

FIGURE 3.14: Tapers optimization for different input waveguide widths. (A) W1=100µm; (B) W1=70µm; (C) W1=50µm; (D) W1=35µm. Sweeps are performed on the taper length while different curves on the same graph refer to different taper profile.

the transmission of the higher taper's TM modes are much lower than the fundamental one. By decreasing W1, the oscillatory behavior is almost completely lost and the conversion is much more efficient.

From the results attached in Fig.3.14, the internal transmission of the tapers present in the samples are around 17%, too small to be useful in applications. Keeping the width W1=100µm and L=100µm, the only degree of freedom is the shape. With m=0.3 it can be increased up to 23.6% but it is still rather small. The best choice is to decrease the taper width up to 35µm. Retaining the linear shape and the initial taper length, there is a dramatic increment in the transmission that passes from 17% to 71.5% with W1=35µm. Moreover, a very slight change on the length is required to make the transmission pass from 71.5% to 96%. This can be achieved with L=165µm, which is a good compromise between transmission and length of the taper. By using m=1.5 and L=190µm the transmission can be further increased to 98%. However, in terms of free carrier absorptions, an increment of 25µm on the taper length could counterbalance the 2% of amelioration in the taper transmission causing the overall transmission to remain unchanged or even worsened . Thus, the best choice is to keep the taper as short as possible but still with a good transmission percentage. Hence a 96% of transmission, L=165µm and W1=35µm is a satisfying result.
It is noteworthy the fact that, when W1/W2 is close to one, i.e. for small values of the input taper, a change in the taper profile does not produce a remarkable change in the transmission (Fig.3.14d). This is because the taper's angle is not so much affected by such a change hence, in this condition, the driving parameter is the length L. A completely different situation instead is found for very large values of the taper's input width, Fig.3.14a, where for short lengths the driving parameter is m.

Conclusions. The analysed results concern just the 5x3µm WG but similar results are expected for the 3x3 one. Moreover, for what concern the 10x3 and 15x3, since the ratio W1/W2 is smaller, the transmission is higher at fixed m,L and W1 with respect to the 3x3 and 5x3 WGs. Hence, a more convenient length of the taper is expected to be obtained for the optimization of the two widest WGs tapers.
For the next fabricated samples, it will be necessary to decrease the input of the taper to 35µm in order to obtain an higher transmission and ameliorated coupling losses. A change in the length is in principle useful because this allows to reach 96% or 98% of internal transmission. Nevertheless, the decision on how much should the length be increased should be taken after having obtained information on the residual doping coming from the fabrication processes: if it is sufficiently small, after the computation of the free carriers absorption losses (as done in section 3.2.4), it will be clear whether or not to lengthen the taper structure or to keep it as 100µm so as not to worsen the losses due to absorption phenomena.

Chapter 4

Experimental setup

This section describes the optical characterization setup that will be used for integrated modulators. During my internship I participated to build the preliminary setup that injects and collects Mid-IR beam into integrated waveguides. A further upgrade of the setup will add the RF section.

The first step is to characterize the passive waveguides described in section 2 and 3. The aim of the characterization is to measure the optical losses.

A schematic image of the optical setup that will be used for the measurements is shown in Fig.4.1. The losses characterization will be based on a direct focus of the QCL, emitting at 8.5µm, on the waveguides tapers input by means of mid-infrared objective lenses. Then, at the output of the waveguides, the light will be collected by another identical objective lens and it will be sent toward two different detectors: a thermal powermeter and an MCT infrared photodetector. There will also be a mid-infrared camera with which it is possible to image the light coming from the waveguides output facets.

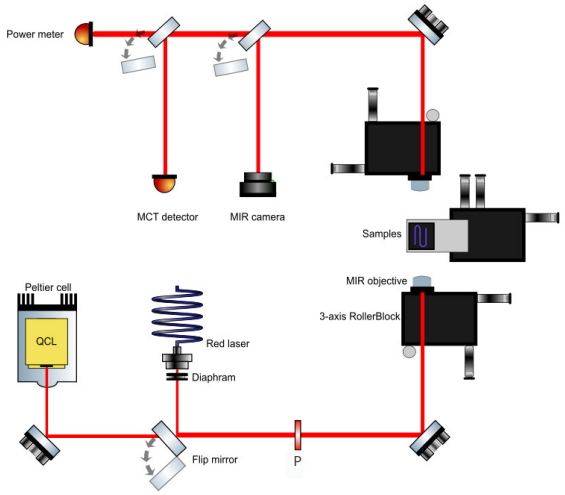

FIGURE 4.1: First optical setup used for the characterization of the integrated MIR amplitude modulators.

4.1 Sources

QCL laser: The mid-IR source used in the experimental set-up is a distributed feedback quantum cascade laser designated for operation between 8.0 to 9.0 µm [25]. My fist task was wire the QCL, mount it on a high cooling Peltier stage (first Peltier stage is integrated on the laser mount) and characterize the QCL features. The Fig.4.2a gives the measured power-current curve as well as the voltage-current curve at 20°C (from the data-sheet, 20° should correspond to a wavelength emission of 8.5µm). The threshold current is about 340 mA and the maximum collected power of 50mW for 400 mA. These values are in good agreement with manufacturer data-sheet. Afterwards, the output laser beam was analyzed in a Fourier transform infrared spectroscopy (FTIR) setup. The Fig.4.2b gives the associated emitted spectrum. It shows a single emission line at 8.499µm(in terms of wavenumber is 1176.3).

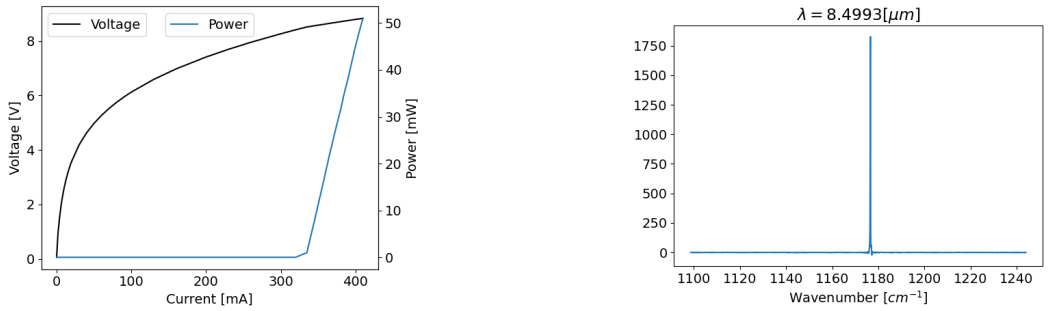

(A) (B)

FIGURE 4.2: QCL characterization. (A): Voltage and output power vs laser drive current; (B) FTIR measurement of the laser emission wavelength.

Red laser: The red laser helps to set a coarse alignment of the beam and it is collinear with the quantum cascade laser.

4.2 Opto-mechanical components

3-Axis RollerBlocks: Used to control the position of the objective lenses and also of the samples with extreme accuracy. They allow to control the position along x, y and z with a micrometric or sub-micrometric resolution. The supports of the objective lenses are equipped with differential micrometers. The coarse adjuster has a resolution of 5µm while the fine adjuster has resolution of 0.5µm. This resolution make these stages ideal for optimizing the coupling efficiency in a waveguide alignment. The supports of the samples are instead equipped with normal micrometers, guaranteeing high stability and high load capacity but without the high resolution of actuators that is instead necessary for the alignment of the objective lenses [26].

Mirrors: Mid-infrared gold mirrors with an average reflectance larger than 98% for 2µm<λ<20µm for angles of incidence in between 0° and 45° [27].

Polarizer: The laser described in the previous section emits TM polarized light. Despite this, even for future use, it will be necessary to insert a polarizer in the setup, which allows only light to pass with a well-defined polarization. Moreover, a direct change of the power on the laser could induce an undesired heating of the device, causing a variation in the emission wavelength. To avoid this, the polarizer can be used also as a density filter just by rotating it, so to tune the power injected in the waveguides. The chosen one is a KRS-5 polarizer [28], with a transmission of roughly 75% around 8.5µm for TM polarizations.

MIR objective lenses: Used to focus and collect the light in and out from the waveguides [29]. They are based on zinc-selenide and are optimized to work with wavelengths in between 2 and 12 µm. They can work with beam diamteres up to 5mm. The laser described in section 4.1 has a beam diameter of 2-3mm. The purchased lens has a focal length of 12mm and, with a beam diameter of 2-3mm at 8.5µm, it gives a beam of 30µm in the focus of the lens. Hence, for samples accurately positioned in the lenses focus, the input beam has 30µm of diameter that is the value used as waist diameter in the FDTD simulations of the waveguides described in the simulations chapter. In this working conditions, the transmission of the lens is aroung 95%, that must be taken into account when measuring the losses of the samples, since the lenses losses are included in the detectors measurements.

Optical microscope: An optical microscope (not sketched in the optical setup figure) is used in order to correctly align and position the waveguide samples.

4.3 Detectors

Thermal power meter: Used to align the red and MIR lasers. It is used to detect relatively high average power (mW of output power).

MCT infrared photodetector: Mercury-Cadmium-Telluride photodetector, used to detect peak power of the order of tens of µW. The detection is done with lock-in technique with a maximum of 100kHz frequency.

MIR camera: Used to visualize the waveguide Mid Infared output beam.

Chapter 5

Conclusions and perspectives

Conclusions. The work done during the internship was extremely formative in understanding how the design of a device works and what are the trade-offs to consider in order to achieve a satisfactory result. Low-loss dielectric waveguides were central in the internship work, since are of primary importance for the success of the project. The investigations through simulations were important to understand the physics of the waveguides, the parameters to be modified for optimization, how to establish a good setting for future simulations and, above all, in which direction the design of the future samples (that will no longer be test samples but will be the first real samples to be made for the project) must be sent. Their validity will then be confirmed or confuted by the results of future measurements.
From the analysis shown in this report, the most contribution to the waveguide losses is mainly determined by the absorption losses, that must be kept well below 7cm^{-1} to allow light to be transmitted in very long structures. Hence, it will be of primary importance to limit the background doping coming from the fabrication processes. The realized samples show also consistent radiation losses and, for the multimode waveguides, consistent field distortion induced by the bends. As a consequence, monomode WGs must be produced or design solutions are required to avoid higher order modes to be excited at the output of the WGs. From the examined waveguides, it is expected that the 5x3µm WG is the most promising one from the experimental point of view, on which the design of the future waveguides might be based. For what concern the coupling losses, the samples have tapers that are not optimized for the transmission hence the best solution is to decrease the input waveguide width to $35\mu m$ and slightly increase the taper length from 100 μm to $165\mu m$ in order to pass from 17% to 96% of transmission. This design optimization will be tested in future samples to be fabricated. Other analyzes that have not been included in the report because they have not yet been completed and will be developed until the end of the internship are the design of the active region of the modulator to be combined with Lumerical simulations implementing the theoretical model described in the appendix A.3 to design the light-matter interaction of the MQWs structure (these results are still uncertain or in any case at an early stage. A brief summary is described in appendix A.3). For what concern the optoelectronic characterization of the WGs, the measurements will be performed until the end of the internship and will be important to validate the simulations and also to validate the assembly and alignment of the optical setup components.

Perspectives and future steps. In the future it will be crucial to start combining the different building blocks analyzed during the internship: in fact, it is not possible to decouple the design of the waveguide from the design of the modulator, everything should be merged together because the trade-off and issues to solve for the optimization of the waveguides are not independent of the ones concerning the active region of the modulator. To achieve the modulation, the active region must be doped and this is detrimental for the waveguide transmission therefore it will be necessary to find a good compromise between the two. Another step would be the introduction of the metallic electrodes in the waveguides simulations: they will introduce further losses since metallic materials exhibit high dissipations that cannot be neglected if the overlap between the electromagnetic field and the electrodes is consistent. A probable solution would be to increase the thickness of the waveguide in fact the thicker the structure, the farer are the electrodes and the lower will be the dissipations introduced by the electrodes but the higher will be the required field to achieve the same modulation depth. The WG structure can be made in different ways, for instance by the MQWs alone or the MQWs could be sandwitched between two cladding layers to further increase the confinement of the field. Another important step will be the definition of the materials to be used to realize the different part of the device. Achieve high modulation rates also requires a careful design of the overall modulator devices, radio frequency simulations (from 100 MHz to 10GHz) of the device has to be carried out in order to guarantee the high speed operation, taking into account the device size and the input RF electrodes as well as the RC constant of the overall device.

Appendix A

Theoretical background

This appendix offers a brief analysis of the physical concepts that are important for understanding the physics of the device described in section 1.3.3, the physics of the waveguides used in the simulations and the optical model of the modulator that will be used in future, giving a hint about the next simulations.

A.1 Intersubband Physics in semiconductor quantum wells

Unlike the majority of electronic devices, which are silicon based, optoelectronic devices are predominantly made by III–V semiconductor compounds such as GaAs, InP, GaN, GaSb, and their alloys (like $Al_xGa_{1-x}As$, with x the molar fraction of Al in the compound) due to their direct-band gap. With the development of epitaxial growth techniques, such as the molecular beam epitaxy (MBE), it has been possible to reach the atomic-layer control of layer thicknesses and to give birth to the concept of *band gap engineering* [30]. The formation of low-dimensional systems, where the electronic wavefunction is confined in one or more dimension, has been a major topic of semiconductor physics in the last three decades. This occurs in the so called *heterostructures*, in which a thin semiconductor layer ($\sim$100Å) is embedded in between two wider band gap semiconductors (notice: to avoid mechanical stress in the formed heterostructure it is fundamental to use lattice matched materials). Depending on the relative bands offsets of the two different materials, the carriers can be confined in one direction inducing the quantization of the energy levels along the direction of the confinement (which is normally the one orthogonal to the growth of the heterostructure). The relative positions between these energy levels can be tuned by changing the depth and the width of the QW. The single band of the bulk material(e.g. the conduction band) thus becomes formed by concentric paraboloids whose vertices are found on each quantized energy level in the direction of the confinement. These paraboloids are denoted *subbands* and transitions occurring across them are called *intersubband transitions* (ISB).

A.1.1 Energy eigenvalues

For the description of the behavior of carriers in an heterostructure is normally used the envelope function approach in the Kane approximation [30]. The wavefunction of the electron can be factorized in the product between a Bloch function of band ν at the centre of the Brillouin zone $u_\nu(\vec{r})$ (encoding all the information concerning the lattice periodicity) and an envelope function $f_i(\vec{r})$ supposed slowly varying on a lattice period (i denotes the quantum number of the problem):

$$\psi_i(\vec{r}) = f_i(\vec{r})u_\nu(\vec{r}) \tag{A.1}$$

In the Kane approximation, all the information concerning the band structure of the material are encoded in the effective mass m^*. This simplification allows to describe the electron's behavior in the heterostructure by a slow-varying envelope function $f_i(\vec{r})$ satisfying the usual Schrödinger's equation:

$$-\frac{\hbar^2}{2m^*}\nabla^2 f_i(\vec{r}) + V(\vec{r})f_i(\vec{r}) = E_i f_i(\vec{r}) \tag{A.2}$$

If the growth direction is taken as the z direction, then the motion is still free along the xy plane and the envelope function can be factorized as a plane wave on xy plane and a function describing the eigenstates along the growth direction. The periodic potential is seen by the particle just along z hence $V(\vec{r}) = V(z)$:

$$f_{i,\vec{k}_\perp}(\vec{r}) = \frac{1}{\sqrt{A}} e^{i\vec{k}_\perp \cdot \vec{r}} \varphi_i(z) \tag{A.3}$$

where $\vec{k}_\perp$ denotes the two dimensional vector (k_x,k_y) and A is the area. The Schrödinger's equation thus becomes:

$$-\frac{\hbar^2}{2m^*}\frac{d^2\varphi_n}{dz^2} + V(z)\varphi_n(z) = E_n\varphi_n(z) \tag{A.4}$$

The equation must be solved in each layer of the heterostructure followed by matching conditions at each interface (Bastard's conditions [31]). In the end, the energy that an electron can have in the heterostructure is described by the following formula:

$$E_{i,\vec{k}_\perp} = E_i + \frac{\hbar^2\vec{k}_\perp}{2m^*} \tag{A.5}$$

Where E_i are the quantized eigenvalues due to the confinement and band edges discontinuity, whose values depend on the shape of $V(\vec{r}) = V(z)$.

A.1.2 Intersubband transitions and light matter interaction

An extensive description of the topic can be found in [30] hence only the paramount formulas, concepts and quantities relevant to the description of the ISB transitions will be treated. To study the interaction between an external electromagnetic field and the heterostructure it is possible to use the Fermi's golden rule in the dipolar approximation (i.e. wavelength much larger than the QW dimension) to compute the transition rate between an initial and final state (i and f respectively).

$$W_{if} = \frac{2\pi}{\hbar}\frac{e^2E_0^2}{4m^{*2}\omega^2}|\langle i|\vec{e}\cdot\vec{p}|f\rangle|^2\delta(E_f - E_i - \hbar\omega) \tag{A.6}$$

After having carried out the calculation and made it explicit, the dipolar term can be written in the following way by exploiting the properties of the Bloch functions and the slowly varying envelope function:

$$\langle i|\hat{e}\cdot\vec{p}|f\rangle = \hat{e}\cdot\langle u_\nu|\vec{p}|u_{\nu'}\rangle\left\langle f_i \mid f_j\right\rangle + \hat{e}\cdot\langle u_\nu \mid u_{\nu'}\rangle\left\langle f_i|\vec{p}|f_j\right\rangle \tag{A.7}$$

where ν, ν', i and j are the band and subband indices of the initial and final states respectively. The first term describes the interband transitions which are accompanied by a change in the band index ν. The second term is instead the one in which we are interested in, i.e. the intersubband transitions term, with the same band index. From the evaluation of the dipole matrix element of the envelope functions it emerges that only the term containing the z component of the field is non-zero. As a consequence, the relevant matrix element for the ISB transitions is:

$$\langle i\,|p_z|\,j\rangle = \int dz\varphi_i^*(z)p_z\varphi_j(z) \tag{A.8}$$

This result implies the well-known *polarization selection rule* of the ISB transitions: optical transitions between confined states in QWs can be excited only by an electric field having a non-zero component along the heterostructure growth direction. The most important consequence is that, in order to couple with ISB transitions, light must be TM-polarized, i.e. with a non zero component perpendicular to the 2D semiconductor layers. This explains why the experiments in the early AMD based on ISB transitions ([13]) have been done with light incident at the Brewster's angle. However, as already explained in section 1.3.4, the strength of the coupling is rather small leading to poor efficient process. It is for this reason that a waveguide geometry is a good solution to increase the light-matter interaction.

A.2 Waveguides

In PICs photons it is desirable that waves propagate in only one direction, say z, while the field is appreciable only in a neighborhood of it. This behavior can be obtained by injecting the electromagnetic wave inside a waveguide. In the project, just dielectric waveguides are used, i.e. WGs that are built with different dielectric materials. The most common, which is also the ones present in the samples shown in chapter 2, are the rectangular strip WGs. Light is normally trapped in the core, a material with higher refractive index with respect to its surrounding, thanks to total internal reflection (TIR): light encountering an intersection

between two materials with different refractive indices (in internal reflection) at a specific angles of incidence can be totally reflected with virtually no losses. The core is usually deposited above a substrate that performs the bottom confinement while the lateral and top confinement is done by air.
In a waveguide, just a finite number of electromagnetic waves are able to propagate. These waves are called *eigenmodes* because in the transverse plane with respect to the propagation direction their profile does not change during the propagation. Their properties depend on the dimensions of the waveguide, the frequency of the light and the refractive indices of the WG materials. Mathematically, one can derive the propagating modes from Maxwell's source-free equations:

$$\nabla \cdot \vec{E} = 0 \qquad \nabla \cdot \vec{B} = 0$$
$$\nabla \times \vec{B} = \frac{1}{c^2}\frac{\partial \vec{E}}{\partial t} \qquad \nabla \times \vec{E} = -\frac{\partial \vec{B}}{\partial t}$$

Based on the Maxwell's curl equations, vectorial wave equations for the electric field $\vec{E}$ and magnetic field $\vec{H}$ can be derived. By choosing z as the propagation direction, the refractive index profile can be written as n = n(x,y). Moreover, by also assuming an infinite dimension along the direction of propagation and that the components of the fields do not have a z-dependence, the Maxwell's equations split into two independent sets of equations composed of three vector quantities each which can be solved in the x-y plane only. These are termed the TE (transverse electric), and TM (transverse magnetic) equations. These two sets of equations lead to the Helmholtz's equations for TE and TM waves. To solve them, BCs at the interfaces between two different materials must be imposed, namely the continuity of the tangential fields and of the normal dielectric displacement and magnetic inductance. The solutions of the problem are the *modes of propagation*. They are defined as propagating or evanescent waves of which the transversal shape (xy plane) does not change during propagation. The effective index n_{eff} of the mode, that is also the square root of the eigenvalues of the problem, contains all the most important information concerning the properties of the mode like the propagation constant, the losses and also information concerning the confinement. The guided modes are discretized and their n_{eff} is higher than the substrate and cladding materials but smaller than the core one. Besides the guided modes there are also the *radiating modes*. Radiating modes show an oscillating behaviour along at least one side of the waveguide structure. Depending on their effective refractive index they are classified as *propagating* or *evanescent* radiating modes. In the last case the effective refractive index is purely imaginary. Guided and radiating modes form a complete set of functions. This means that every field inside the waveguide can be represented by a sum of these modes.

Solutions for which n_{eff} is smaller than the substrate one but higher than the cladding are called *propagating radiative modes* and they are no longer confined just in the core but spread all over the substrate. If n_{eff} is also smaller than the cladding than the mode is named *evanescent radiating mode*

A.2.1 Losses in dielectric waveguides

One of the objective of the project is to realize low-loss MIR dielectric waveguides. There are different causes for these losses: the light-matter interaction gives the absorption phenomenon while non perfect guiding structures result in scattering and radiation losses. When the origin of the loss is uniformly spread over the waveguide length, the guided optical power will decrease exponentially with the propagation distance, i.e. $P(z)=P(0)e^{-\alpha z}$, with α the absorption coefficient per unit of length, usually in cm^{-1}.

Interband and free carriers absorption

In direct band gap semiconductors, like III-V semiconductors, the easiest way to have losses due to absorption is with electron-hole pair creation by photons with energy higher than the band gap energy. In this specific case, however, since the device is optimized to work at 8.5µm (which corresponds to roughly 146meV), the photon energy is much smaller than the band gap energy of the material used for the waveguides (see chapter 3) hence the major cause of absorption losses is the free carriers absorption: due to the fact that usually the samples have residual doping coming from the fabrication processes, there are free carriers in the conduction band of the material that can easily absorb photons of small energies and be promoted to higher energy states (in plane absorption that can be included in the optical response description using a Drude model). As shown in section 3.2.4, this is one of the most important limitation to be overcome for the

MIR applications, especially at such large wavelengths. Moreover, absorption due to metal in proximity as well as surface absorption in non-passivated WGs can give a further contribution in absorption losses.

Scattering

Scattering losses are caused by spatial fluctuations of the refractive index (volume scattering) or by the roughness at the sidewalls of the waveguide (surface roughness scattering). These can be both etched waveguide boundaries that determine the waveguide or the interface of two layers which are grown on top of each other. Surface scattering is proportional to the squared values of the electric field at the surfaces of the core. Nevertheless, since the dimension of the surface roughness is extremely small if compared to the working wavelength, this issue can be neglected with respect to the former one.

Radiation losses

Loss through radiation is due to the non perfect guiding of the waveguide. With no total internal reflection (i.e. below the cut-off) the power will leak out of the WG.
Bent waveguides show a fundamental radiation loss. They represent another major limitation for MIR waveguide applications and, in order to be avoided, requires a subtle and precise design of the waveguide. In straight waveguides the tendency for light to diffract is compensated by the higher refractive index of the waveguide core and the waveguide mode has flat phase fronts. In bent waveguides the phase front is rotating around a rotation center. Because the group velocity of the phase fronts can not exceed the local speed of light (c/n), there is a point where the phase front bends and where radiation occurs. Moreover, they increase nearly exponentially with decreasing bend radius. It is worth to notice that in bent WGs the lossless guided modes are the ones that become lossy. The mode profile in the bend will shift toward the outer edge of the bent section. As a consequence, at the transition from straight to bent waveguide, mode adaptation losses will occur, leading to scattering at the abrupt radius transition regions (start and end of fixed radius bends).

A.3 Optical properties of a multiple quantum well structure: the effective medium approach

As already analyzed in section 1.3.3, the active region of the device will consist of a multiple quantum well structure. Moreover, it is necessary to have a model that describes the coupling of infrared light to ISB transitions in this kind of structure to be used for the design and the simulations of the amplitude modulator. To this aim, an effective medium approach is used to define an effective dielectric function, useful for the description of MQWs-light interaction. The model ([1], [32]) is valid in the long-wavelength limit (wavelength much larger than the MQW dimension) and describes the MQW structure as an anisotropic uniaxial dispersive medium where the dielectric function is defined as a diagional tensor:

$$\varepsilon(\omega) = \begin{pmatrix} \varepsilon_{xx}(\omega) & 0 & 0 \\ 0 & \varepsilon_{xx}(\omega) & 0 \\ 0 & 0 & \varepsilon_{zz}(\omega) \end{pmatrix} \tag{A.9}$$

The term $\varepsilon_{xx}(\omega)$ describes the in plane absorptions and is mainly determined by two different phenomena. The first is the free carriers absorption ascribed to the presence of carriers in the bottom of the conduction band because of the doping (which is necessary in the AMD to achieve the modulation effect). This is substantially described by a Drude model. The second is instead ascribed to the presence of the optical phonons. In III-V semiconductors, like GaAs and AlGaAs, the atoms are arranged in a zinc-blende crystalline structure by covalent bonds. The chemical bond shows a partial ionic character because of the electronegativity difference between the atoms involved in the bond, inducing a polarity due to the asymmetric electronic cloud. Thus, a dipole moment is present and it can interact with an external EM field. This is the reason why covalent polar crystals show strong absorption and reflection bands in the infrared spectral range when the frequency is close to transverse optical (TO) phonon modes of the crystal. The polar character of the chemical bond makes III-V semiconductors TO phonon modes IR active, a fact that strongly affects the optical response of these materials in the infrared range. The expression of the in plane component can be written as:

$$\varepsilon_{xx}(\omega) = \epsilon_{xx} + \Delta\varepsilon_{xx}(\omega) \tag{A.10}$$

where:

$$\epsilon_{xx} = (1-f)\varepsilon_b + f\varepsilon_w \tag{A.11}$$

where ε_b and ε_w are the dielectric functions of the barrier and well materials respectively. They should be defined, in turn, with Lorentzian models accounting for the phononic resonances ([33] for GaAs and [34] for $Al_xGa_{1-x}As$). f is defined as L_{QW}/L_{MQW} where L_{Qw} is the length of the QW and L_{MQW} is the length of the MQW structure in one period. The Drude model is inserted in $\Delta\varepsilon_{xx}(\omega)$:

$$\Delta\varepsilon_{xx}(\omega) = \frac{4\pi e^2 N_s}{\omega^2 m L_{MQW}} \frac{-1}{i(\omega\tau_{||})^{-1}+1} \tag{A.12}$$

where N_S is the doping per unit of area and $\tau_{||}$ is the intrasubband relaxation time. The ISB transition contribution is included in the z-component of the tensor:

$$\frac{1}{\varepsilon_{zz}(\omega)} = \frac{1}{\epsilon_{zz}} - \frac{\Delta\varepsilon_{zz}(\omega)}{\varepsilon_w^2} \tag{A.13}$$

with $(\epsilon_{zz})^{-1}$=(1-f)/ε_b+f/ε_w and:

$$\Delta\varepsilon_{zz}(\omega) = \frac{2\pi e^2 N_s f_{12}\hbar}{\omega m \Gamma L_{MQW}} \cdot \frac{1}{[E_{21}^2 - (\hbar\omega)^2] - i2\hbar\omega\Gamma} \tag{A.14}$$

with f_{12} is the oscillator strength connected with $1 \rightarrow 2$ transition (to be derived from the quantum design); E_{21} is the ISB transition energy that can include also the many body effects like the depolarization shift; Γ is the FWHM of the ISB transition peak. When the modulator is unbiased, absorption cannot occur because there are no electrons populating the right energy level. However, with an applied voltage, due to the tunneling effect, there are electrons that can absorb the photons. This leads to the presence of an atomic-like absorption line which is identified as a Lorentzian in the imaginary part of $\varepsilon_{zz}(\omega)$ while in the real part a sudden index change is seen. The absorption per unit length $\alpha(\omega)$ of the WG amplitude MD is computed as $\alpha(\omega) = -\omega \cdot n/c \cdot Im((\varepsilon_{zz}(\omega))^{-1})$, where n is the background refractive index, c is the speed of light and ω is the working angular frequency. The model has been implemented in python and an example is provided in Fig.A.2.

The first result of the solution of the self-consistent Schrödinger-Poisson equation is shown in Fig.A.1, where a simple undoped and unbiased structure has been considered. From such simulation it is possible to extract the oscillator strength associated to the transmission and all the parameters to be defined in the model in [1] that depend on the band diagram. This analysis must be developed in details until the end of the internship. To start analyzing these new concepts, the effective index approach has been implemented in FDTD simulations in Lumerical to mimic the behavior of the modulator. To this aim, a new material with permittivity defined in Eq.A.9 has been defined in the simulation setting, with the required values taken from [1]. The core is made by the MQWs and the substrate is InP with n=3. The source excites the fundamental TM mode and the overall simulation features are the same as in the straight WGs FDTD simulations described in 3.2.2. Different lengths of the modulator (denoted with W) have been investigated to see how the tranmsission changes as function of the length. To simulate the zero bias condition, the oscillator strength f_{12} in Eq.A.14 has been set to zero. The result is shown in Fig.A.3b, where the modulation depth can be computed. As the length increases, the absorption increases but the peak becomes broader and shifts at higher wavelengths.

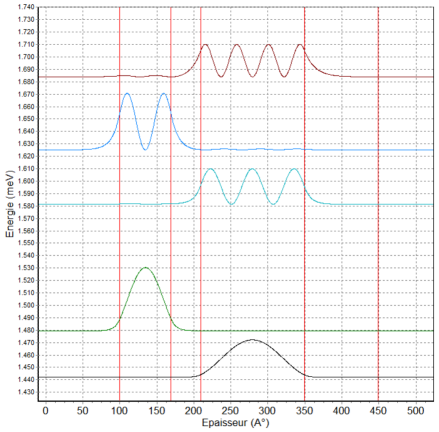

FIGURE A.1: First band diagram computation of a coupled quantum wells system made of $Al_{0.33}Ga_{0.67}As/GaAs$. No doping has been considered in this structure. The width of the smallest well is 69Å, the widest one is 140Å, the central barrier width is 40Åand for the lateral barriers is 100Å. No bias is applied to the structure. The energy difference between the green and blu levels is 145.85meV, which corresponds to λ=8.5µm.

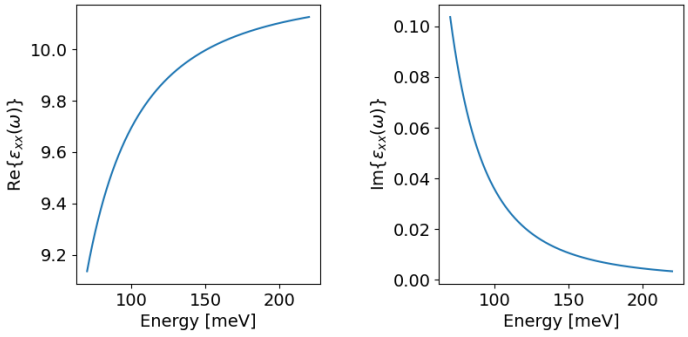

(A) $\varepsilon_{xx}(\omega)$

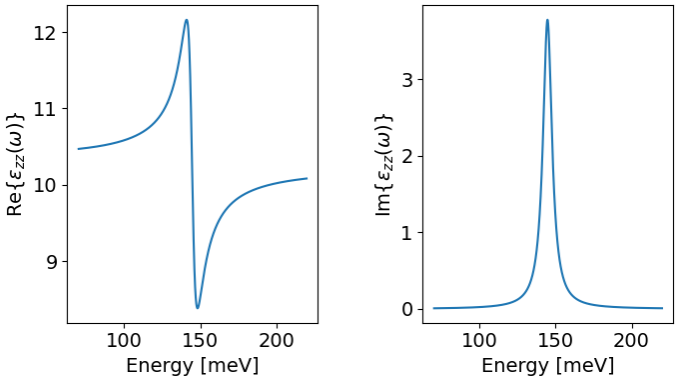

(B) $\varepsilon_{zz}(\omega)$

FIGURE A.2: Real and imaginary parts of the x and z components of the effective dielectric tensor of a MQW structure, with values taken from [1] to reproduce the paper's results.

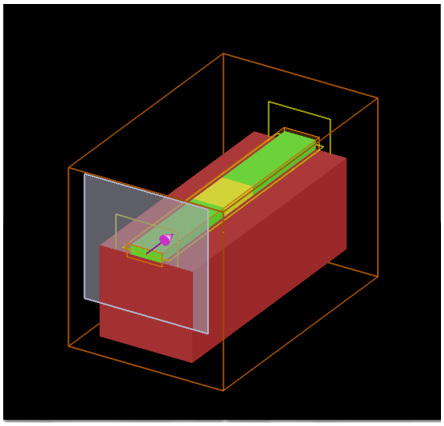

(A)

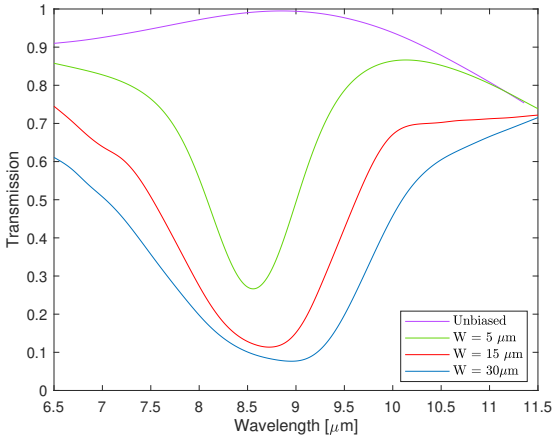

(B)

FIGURE A.3: (A) FDTD simulation region for the modulator. The entire WG is made by the MQWs but only the central region (yellow) is biased; (B) Transmission through output monitor as function of the modulator length.

Appendix B

Bibliography

[1] M. Załużny and C. Nalewajko. Coupling of infrared radiation to intersubband transitions in multiple quantum wells: The effective-medium approach. *Phys. Rev. B*, 59:13043–13053, May 1999.

[2] E.A. Saleh and Malvin Carl Teich. Guided-wave optics. In *Fundamentals of Photonics*, chapter 7, pages 238–271. John Wiley & Sons, Ltd, 1991.

[3] Robert G. Hunsperger. *Integrated Optics*. Springer New York, 2009.

[4] Larry A. Coldren and S.W. Corzine. *Diode Lasers and Photonic Integrated Circuits*. Wiley, 1995.

[5] Jerome Faist, Federico Capasso, Deborah L. Sivco, Carlo Sirtori, Albert L. Hutchinson, and Alfred Y. Cho. Quantum cascade laser. *Science*, 264(5158):553–556, 1994.

[6] Yu Yao, Anthony J. Hoffman, and Claire F. Gmachl. Mid-infrared quantum cascade lasers. *Nature Photonics*, 6:432–439, 2012.

[7] B. F. Levine. Quantum-well infrared photodetectors. *Journal of Applied Physics*, 74(8):R1–R81, 1993.

[8] Stefano Pirotta, Ngoc-Linh Tran, Arnaud Jollivet, Giorgio Biasiol, Paul Crozat, Jean-Michel Manceau, Adel Bousseksou, and Raffaele Colombelli. Fast amplitude modulation up to 1.5 ghz of mid-ir free-space beams at room-temperature. *Nature Communications*, 12:799, 2021.

[9] Borislav Hinkov, Jakob Hayden, Rolf Szedlak, Pedro Martin-Mateos, Borja Jerez, Pablo Acedo, Gottfried Strasser, and Bernhard Lendl. High frequency modulation and (quasi) single-sideband emission of mid-infrared ring and ridge quantum cascade lasers. *Opt. Express*, 27(10):14716–14724, May 2019.

[10] `https://gandh.com/product-categories/acousto-optic-modulators/`.

[11] `https://www.qubig.com/`.

[12] Etienne Rodriguez, Alireza Mottaghizadeh, Djamal Gacemi, Daniele Palaferri, Zahra Asghari, Mathieu Jeannin, Angela Vasanelli, Azzurra Bigioli, Yanko Todorov, Mattias Beck, Jerome Faist, Qi Jie Wang, and Carlo Sirtori. Room-temperature, wide-band, quantum well infrared photodetector for microwave optical links at 4.9 μm wavelength. *ACS Photonics*, 5(9):3689–3694, 2018.

[13] V. Berger, N. Vodjdani, D. Delacourt, and J. P. Schnell. Room-temperature quantum well infrared modulator using a schottky diode. *Applied Physics Letters*, 68(14):1904–1906, 1996.

[14] J. Y. Duboz, V. Berger, N. Laurent, D. Adam, and J. Nagle. Grating coupled infrared modulator at normal incidence based on intersubband transitions. *Applied Physics Letters*, 70(12):1569–1571, 1997.

[15] N. Vodjdani, B. Vinter, V. Berger, E. Böckenhoff, and E. Costard. Tunneling assisted modulation of the intersubband absorption in double quantum wells. *Applied Physics Letters*, 59(5):555–557, 1991.

[16] E. Dupont, D. Delacourt, V. Berger, N. Vodjdani, and M. Papuchon. Phase and amplitude modulation based on intersubband transitions in electron transfer double quantum wells. *Applied Physics Letters*, 62(16):1907–1909, 1993.

[17] Hamza Dely, Thomas Bonazzi, Olivier Spitz, Etienne Rodriguez, Djamal Gacemi, Yanko Todorov, Konstantinos Pantzas, Grégoire Beaudoin, Isabelle Sagnes, Lianhe Li, Alexander Giles Davies, Edmund H. Linfield, Frédéric Grillot, Angela Vasanelli, and Carlo Sirtori. 10 gbit s1 free space data transmission at 9 µm wavelength with unipolar quantum optoelectronics. *Laser & Photonics Reviews*, 16(2):2100414, 2022.

[18] Seungyong Jung, Daniele Palaferri, Kevin Zhang, Feng Xie, Yae Okuno, Christopher Pinzone, Kevin Lascola, and Mikhail A. Belkin. Homogeneous photonic integration of mid-infrared quantum cascade lasers with low-loss passive waveguides on an inp platform. *Optica*, 6(8):1023–1030, Aug 2019.

[19] Jeff Chiles, Nima Nader, Eric J. Stanton, Daniel Herman, Galan Moody, Jiangang Zhu, J. Connor Skehan, Biswarup Guha, Abijith Kowligy, Juliet T. Gopinath, Kartik Srinivasan, Scott A. Diddams, Ian Coddington, Nathan R. Newbury, Jeffrey M. Shainline, Sae Woo Nam, and Richard P. Mirin. Multifunctional integrated photonics in the mid-infrared with suspended algaas on silicon. *Optica*, 6(9):1246–1254, Sep 2019.

[20] `https://support.lumerical.com`.

[21] E. A. J. Marcatili. Bends in optical dielectric guides. *Bell System Technical Journal*, 48(7):2103–2132, 1969.

[22] Lukas Chrostowski and Michael Hochberg. *Silicon Photonics Design: From Devices to Systems*. Cambridge University Press, 2015.

[23] Andrea Melloni, Paolo Monguzzi, Raffaella Costa, and Mario Martinelli. Design of curved waveguides: the matched bend. *J. Opt. Soc. Am. A*, 20(1):130–137, Jan 2003.

[24] A. Melloni, F. Carniel, R. Costa, and M. Martinelli. Determination of bend mode characteristics in dielectric waveguides. *Journal of Lightwave Technology*, 19(4):571–577, 2001.

[25] `https://www.thorlabs.com/thorproduct.cfm?partnumber=QD8500HHLH`.

[26] `https://www.thorlabs.com/newgrouppage9.cfm?objectgroup_id=1953&pn=RBL13D`.

[27] `https://www.thorlabs.com/newgrouppage9.cfm?objectgroup_id=12178&pn=PF10-03-M02-10#12194`.

[28] `https://www.thorlabs.com/newgrouppage9.cfm?objectgroup_id=1118&pn=WP25H-B#3265`.

[29] `https://www.edmundoptics.fr/f/zinc-selenide-infrared-ir-focusing-objectives/14361/`.

[30] Manfred Helm. The basic physics of intersubband transitions. In H.C. Liu and Federico Capasso, editors, *Intersubband Transitions in Quantum Wells: Physics and Device Applications I*, volume 62 of *Semiconductors and Semimetals*, chapter 1, pages 1–99. Elsevier, 1999.

[31] G. Bastard. Theoretical investigations of superlattice band structure in the envelope-function approximation. *Phys. Rev. B*, 25:7584–7597, Jun 1982.

[32] J.-M. Manceau, S. Zanotto, T. Ongarello, L. Sorba, A. Tredicucci, G. Biasiol, and R. Colombelli. Mid-infrared intersubband polaritons in dispersive metal-insulator-metal resonators. *Applied Physics Letters*, 105(8):081105, 2014.

[33] EDWARD D. PALIK. Gallium arsenide (gaas). In EDWARD D. PALIK, editor, *Handbook of Optical Constants of Solids*, pages 429–443. Academic Press, Boston, 1985.

[34] O.J. GLEMBOCKI and KENICHI TAKARABE. Aluminum gallium arsenide (alxga1xas). In EDWARD D. PALIK, editor, *Handbook of Optical Constants of Solids*, pages 513–558. Academic Press, Boston, 1998.